Check for updates

A laboratory study on the uptake of gaseous molecular iodine by clay minerals at different relative humidities†

Shuzo Kutsuna [iD] * and Naoki Kaneyasu [iD]

Dry deposition of iodine is a crucial parameter for estimating the public health risk of radioiodine released in the Fukushima Dai-ichi nuclear power plant accident. We measured the uptake of molecular iodine (I_2) by aqueous solutions and clay minerals in the laboratory to inform estimates of the ground surface resistance for I_2 in dry deposition which photolysis limited to nighttime. We injected rectangular pulses of humidified air including I_2 into a contactor holding samples of aqueous solutions and clay minerals and monitored I_2 concentrations in air leaving the contactor to distinguish I_2 loss from I_2 adsorption. Uptake of I_2 proceeded much more rapidly by aqueous ascorbic acid than by water; the former was limited by mass transfer in the gas-film layer. Uptake of I_2 by clay samples was confirmed under dry conditions (20−80% relative humidity), which suggested that it contributed to the dry deposition of I_2 onto soils as much as other processes such as reactions with organic matter. The surface resistance for I_2 increased with repeated experiments on the same clay samples, reaching 240−670 s m^{-1}, and its dependence on relative humidity differed from that for sulfur dioxide (SO_2), a commonly used proxy for I_2 in scaling methods. Reference values of surface resistance for SO_2 above soils remain useful for estimating the resistance for I_2 above vegetate surfaces at 80% RH in atmospheric transport and dispersion model calculations but may result in substantial errors at 20% RH unless organic matter in soils contributes to ground surface resistance for I_2.

Environmental significance

Ground surface resistance for iodine is a crucial parameter in dry deposition for estimating the public health risk associated with accidental release of radioiodine from nuclear power plants. We conducted rectangular pulse experiments on the uptake of I_2 by clay samples and confirmed I_2 deposition on the clay samples. The deposition rates decreased with successive runs and remained finite through each set of experimental runs. The resultant ground surface resistances for I_2 were greater than the resistances adopted in atmospheric model calculations which considered no difference between I_2 and its photo-degradation products. The relative-humidity dependence was different between these resistances. Radioiodine dry deposition processes therefore need to be estimated separately before and after sunrise when I_2 is released at night.

1. Introduction

Radioiodine-131 (^{131}I), with a half-life of 8 days, is a major contributor to the public health risk associated with accidental release of radionuclides, because of its high short-term radiation levels and the tendency of iodine to concentrate in the thyroid gland.[1] The accident at the Fukushima Dai-ichi nuclear power plant following the 11 March 2011 Tohoku earthquake and tsunami released ^{131}I into the atmosphere in several different forms, including molecular iodine (I_2), methyl iodine (CH_3I), and aerosol-form iodine such as cesium iodide (CsI),[2]

which behave differently in the atmosphere. The atmospheric reaction and deposition processes of these species, in particular the deposition velocity, need to be known so that the emission source terms of radioiodine released in the accident and the inhaled internal dose of radioiodine in affected populations can be properly estimated by atmospheric transport and dispersion models[2,3] from limited field observations.[4−6]

Dry deposition of ^{131}I has been studied in both field releases[7−10] and wind tunnel experiments[11,12] to investigate the transfer from the atmosphere to grass and other surrogate surfaces. Deposition velocities of radioiodine have also been calculated from field observations after the Windscale nuclear accident in 1957[13] and nuclear tests in the atmosphere.[9] Reported deposition velocities of elemental iodine or I_2 onto various surfaces, however, vary from 0.02 to 26 cm s^{-1}.[14] When dealing with atmospheric transport of radioiodine, the

National Institute of Advanced Industrial Science and Technology (AIST), 16–1 Onogawa, Tsukuba, Ibaraki 305 8569, Japan. E-mail: shuzo530@gmail.com

† Electronic supplementary information (ESI) available. See https://doi.org/10.1039/d2ea00039c

© 2022 The Author(s). Published by the Royal Society of Chemistry

Environ. Sci.: Atmos., 2022, **2**, 1041–1059 | **1041**

chemical form of iodine has to be considered explicitly. Because photolysis limits the lifetime of I_2 to about 10 seconds,[15,16] most field studies on the release of I_2 in daytime have reported the behavior of not I_2 itself, but a mixture of iodine species produced through atmospheric reactions initiated by photolysis of I_2.[16] Similarly, in almost all models of the release of radio-iodine from nuclear power plants, the species reported as I_2 include not only molecular iodine but also other potential iodine species, such as HOI, produced by atmospheric reactions; we refer to this mixture as I_2^{model}. In the models applied to the Fukushima accident, deposition velocities of I_2^{model} over short vegetation are assumed to have constant values, such as 0.3 cm s^{-1},[17] or values similar to that of sulfur dioxide (SO_2).[3] If dry deposition velocities of I_2 differ greatly from these values, the dry deposition process of I_2^{model} needs to be estimated separately before and after sunrise when I_2 is released at night.

In numerical models, the dry deposition process is commonly treated as a resistance model, which consists of a series of resistances.[18] The bulk surface resistance, which represents the transfer of substances at the level nearest to Earth's surface, is typically the most uncertain because it involves the atmospheric chemistry of each species over various surfaces, such as leaf cuticles and soils. The bulk surface resistance consists of stomatal resistance and non-stomatal resistance. For I_2, stomatal resistance is ignored because photolysis limits dry deposition of I_2 to nighttime, when most plants close their stomata.[19] Non-stomatal resistance, R_{ns}, above vegetate surfaces is decomposed as

$$\frac{1}{R_{ns}} = \frac{1}{R_{ac} + R_g} + \frac{1}{R_{cut}} \tag{1}$$

where R_{ac} is the in-canopy aerodynamic resistance, R_g is the subsequent ground resistance, and R_{cut} is the resistance to cuticle uptake.[20] For surfaces without canopies, such as bare soil and open water, R_{ac} and R_{cut} are not applicable. When information on R_g and R_{cut} is limited, models commonly estimate these resistances by a scaling method, relying on an effective Henry's law coefficient or a half-redox potential as an index.[20,21] For I_2, however, effective Henry's law coefficients cannot be defined unless the aqueous concentration of I^- in the following reaction is assumed to be constant.

$$I_2 + H_2O \rightleftarrows I^- + HOI + H^+ \tag{R1}$$
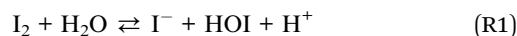
Given these considerations, we conducted a laboratory study of I_2 uptake by various reactors, consisting of six different types of clay mineral particles and three different aqueous surfaces, to provide data for estimating R_g for I_2 above soils. We used a rectangular pulse method[22] to distinguish loss of I_2 from adsorption onto the reactor. This method can be conducted under lower-atmospheric conditions such as humidified air at 1 atm. The pulse method is useful for determining the loss rates for the reactors which tend to deactivate with exposure to I_2 because it can control the exposure to I_2 precisely at low concentration levels of I_2. As a disadvantage, it needs an estimate of mass-transfer resistances in gas-film layers above the solid or the liquid reactors for determination of the surface resistance above the reactors. The clay samples consisted of five pure clay minerals and standard clay soil, and the aqueous surfaces were water, aqueous sulfuric acid, and aqueous ascorbic acid. In this paper we present surface resistances estimated from the experiment and resultant non-stomatal resistances and discuss their implications for calculations in atmospheric transport and dispersion models.

2. Methods

2.1 Materials

Molecular iodine (anhydrous, beads, 10 mesh, 99.999%) was purchased from Sigma-Aldrich. Sodium iodide (99.5%), 1/240 M standard aqueous potassium iodate ($NaIO_3$) solution, 0.5 M standard aqueous sulfuric acid (H_2SO_4) solution, L(+)-ascorbic acid (99.6%), and 1 M standard aqueous sodium hydroxide (NaOH) solution were purchased from FUJIFILM Wako Chemicals. These reagents were used without further purification. Water was purified with an EMD Millipore Milli-Q Gradient A10 system (>18 MΩ cm). Synthetic air (an O_2–N_2 mixture, 1 : 4 volume ratio) and carbon dioxide gas (CO_2, 1.02% in synthetic air) were purchased from Takachiho Chemical Industrial Co., Ltd.

Pure clay minerals of kaolinite, halloysite, montmorillonite, allophane, and illite were purchased from Iwamoto Mineral. These were the same materials used in previous studies at our laboratory.[23–25] Clay powder of AgroMAT Clay Soil AG-1 (Lot No. S131024028, SCP Science) was purchased from GL Science Inc. The allophane and the illite samples were ground to reduce the particle size with a mortar machine. The other clay samples were used as purchased. The grain size of the samples ranged from several millimeters down to submillimeter sizes. Table 1 lists the Brunauer–Emmett–Teller (BET) surface areas of these samples. AgroMAT AG-1 contained organic matter by 3.7% in weight, based on the loss-on-ignition method.

2.2 Experimental setup

The experimental setup is shown schematically in Fig. 1. Each experimental run comprised preparation and injection of an I_2–air mixture of specified relative humidity (RH), passage of the mixture through a two-phase contact chamber (contactor), and analysis of the mixture leaving the contactor in an incoherent broad-band cavity-enhanced absorption spectroscopy (IBB-CEAS) instrument.[26–28] The method for injecting and flowing the gas mixture through the contactor was essentially the same as that reported for volatile organic compounds by the authors.[22] The gas flow was controlled with eight mass-flow controllers (d in Fig. 1) at rates listed in Table S1 in the ESI.† The gas mixtures flowed through perfluoroalkoxy alkane (PFA) tubes covered in black.

2.2.1 Gas mixture preparation and injection. About 5 g of I_2 beads was placed in a PFA bottle (inner diameter, 25.4 mm) in the cavity of the aluminum block of an electronic dry bath (CTU-Mini, Taitec) set at 288.2 K (Fig. 1(a)–(c)). Synthetic air was introduced into the bottle to produce an I_2–air mixture that was further diluted with synthetic air to produce a mixture referred

Table 1 Properties of clay samples

	Kaolinite	Halloysite	Montmorillonite	Allophane	Illite	AgroMAT AG-1
Morphology	Thin sheets	Tubes	Thin sheets	Hollow spherules		
Structure	Crystalline (1 : 1)	Crystalline (1 : 1)	Crystalline (2 : 1)	Amorphous	Crystalline (2 : 1)	
Origin	Kawachi, Tochigi, Japan	New Zealand	Aterazawa, Yamagata, Japan	Kanuma, Tochigi, Japan	Fithian, Ill, USA	
BET area ($m^2 g^{-1}$)	16	29	18	235	70	12
Others	Kanpaku kaolin	Metahalloysite	KUNIPIA-F, Na-type		API no. 35[a]	200 mesh size

[a] Standard clay samples from the American Petroleum Institute, no. 35 (Fithian, Ill).

to hereafter as I_2–air(o). As shown in the ESI,† the partial pressure of I_2 in I_2–air(o), P_{in-o}, was determined by bubbling I_2–air(o) into 20 mL of 20 mM NaOH solution in an impinger (*f*) for a certain time period, followed by analysis of the solution with an ion chromatograph (Dionex ICS-2100, Thermo Fisher Scientific) for I^- and IO_3^- produced through

$$3I_2 + 3NaOH \rightarrow 5I^- + IO_3^- + 3Na^+ + 3H^+ \tag{R2}$$
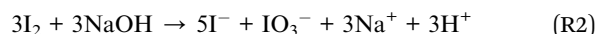
I_2–air(o) was injected using a computer-controlled syringe pump (PSD/4, Hamilton Co.), comprising a 1.25×10^{-2} dm^3 glass gas-tight syringe (*g*) and a three-port ceramic valve (*h*), into the flow of a mixture of 400 ppmv CO_2 and humidified synthetic
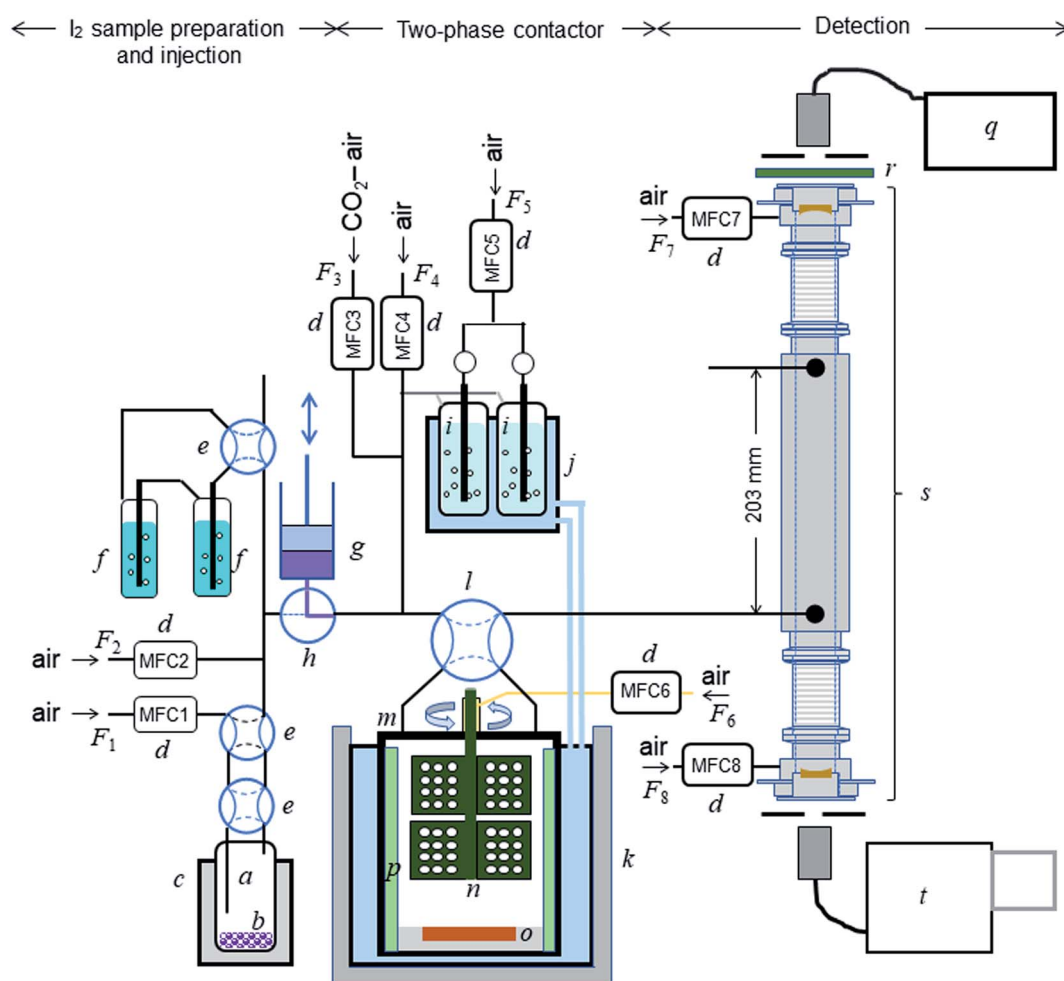

Fig. 1 Schematic diagram of the experimental setup: (a) bottle containing I_2 beads (b); (c) electronic dry bath; (d) mass-flow controllers; (e) four-port valve; (f) impinger with 20 mM NaOH; (g) syringe pump; (h) three-port ceramic valve; (i) humidifier; (j) temperature-controlled water circulator; (k) stainless-steal water bath; (l) four-port valve; (m) contactor; (n) turbine for stirring the gas phase; (o) dish to hold samples; (p) baffles; (q) light source; (r) optical bandpass filter; (s) IBBCEAS measurement cavity; (t) spectrometer.

© 2022 The Author(s). Published by the Royal Society of Chemistry

Environ. Sci.: Atmos., 2022, **2**, 1041–1059 | **1043**

air (humidified at 283.2 K; (i) and (j)); the resulting I_2–CO_2–air mixture is hereafter referred to as I_2–air(s). The syringe pump was shaded with aluminum foil to protect I_2 from photolysis. The syringe pump introduced I_2–air(s) into the contactor as a rectangular pulse of I_2 (pulse width, 300 s; partial pressure, 4 $\times 10^{-7}$ or 2×10^{-7} atm).

2.2.2 Two-phase contactor. The contactor, a cylindrical PTFE vessel (Fig. 1(m): inner diameter, 81 mm; inner height, 80 mm), was almost fully submerged in a jacketed stainless-steel water bath (BT-80, SGI) (k) at 283.2 K; the temperature was maintained by circulating temperature-controlled water (NCB-2100, EYELA) through the jacket. Inside the contactor were a PTFE-coated stainless-steel turbine (n, Yamazaki Seisakusyo), a PTFE dish (80 mm in diameter and 5 mm high) with a central basin (o), and PTFE-coated stainless-steel baffles (p), leaving a remaining gas-phase volume of 0.390 dm³. The turbine consisted of two sets of three blades, arranged vertically and offset by 60°, with each blade containing 12 holes, and stirred the gas phase at 300 rpm. Synthetic air was slowly introduced into the contactor (ca. 2.4×10^{-5} dm³ s⁻¹) through the dead space between the contactor and the axis of the turbine using a mass-flow controller (MFC6 in Fig. 1) to prevent the sample gases from lingering there. The PTFE vessel, its PTFE lid, the support for the motor connected to the contactor, and the PTFE dishes were fabricated in our workshop. Fig. S1† shows the dimensions of the vessel, turbine, baffles, and dishes.

Aqueous solutions were set in dishes with deep basins (4 mm) of two different diameters (30 or 55 mm), and clay samples were set loosely in dishes with shallow (2 mm) basins with diameters of 35 or 55 mm. The ratios between the areas of the basin (S) and the floor of the contactor (S_c), S/S_c, were 0.137 or 0.461 for aqueous solutions and 0.187 or 0.461 for clay samples. The sample sizes depended on the S/S_c as follows: aqueous samples were 2.8 mL for $S/S_c = 0.137$ and 9.4 mL for $S/S_c = 0.461$, and clay samples were 0.73 g for $S/S_c = 0.187$ and 1.78 g for $S/S_c = 0.461$. Before I_2–air(s) was introduced into the contactor, the same gas mixtures without I_2 had flowed over each clay sample for >90 min under the same experimental conditions. A four-port PTFE valve (l) was used to direct I_2–air(s) into the contactor.

2.2.3 Detection and analysis. After passing through the contactor, the gas mixture entered a PTFE cell (Fig. 1(s); inner diameter, 20 mm) for measuring I_2 in the IBBCEAS instrument. The inlet and outlet of the cell were 0.203 m apart, and its ends were equipped with plano-concave mirrors 25 mm in diameter with a 1.0 m radius of curvature (quoted reflectivity > 0.999 at 515 nm; Article 142831, Layertec), forming a stable optical cavity ca. 0.5 m long. To protect the mirrors from I_2 and reduce the residence time of the sample gas in the cell, synthetic air was purged over the mirrors at a constant flow rate (MFC7 and MFC8 in Fig. 1; F7 and F8 in Table S1†).

Light from a laser-driven broadband xenon light source ((q) Model EQ-99-FC, ENERGETIQ) was directed into the cavity through a fiber-coupled output, using a bandpass filter ((r) FF03-525/50-25, Semrock) to exclude light outside the wavelength range of interest (500–550 nm). The light output from the cavity was directed into a spectrograph ((t) M25-GTM, Bunko

Keiki) with a grating of 1200 grooves per mm equipped with a 1024 × 256 pixel CCD camera (DU420-OE, ANDOR). Full vertical binning was applied, providing 1024 superpixels. Spectra were recorded by averaging four spectra taken with exposure times of 1 s (total exposure time of 4 s).

2.3 Quantification of I_2

In IBBCEAS measurements, the relationship between the spectra and the I_2 concentration in the cavity (Fig. 1(s)) is[26]

$$n_{I_2}\sigma_{I_2} = \frac{1 - R_m}{d_{eff}}\left(\frac{I_0}{I} - 1\right) \quad (2)$$

where n_{I2} and σ_{I2} are the number density and absorption cross section, respectively, of I_2; R_m is the mirror reflectivity; d_{eff} is the effective single-pass extinction path length of the I_2–air mixture in the cell; and I_0 and I are the intensity of transmitted light recorded with synthetic air and I_2–air(s), respectively, inside the cavity, with both gases containing CO_2 and water vapor. Letting $P_{out}(t)$ be the partial pressure of I_2 in the I_2–air(s) leaving the contactor at time t, eqn (2) yields

$$P_{out}(t) = \frac{\frac{I_0}{I_{out}(t)} - 1}{\frac{I_0}{I_{in}(t)} - 1} \times P_{in} \quad (3)$$

where $I_{out}(t)$ is the I value at time t for I_2–air(s) leaving the contactor, $I_{in}(t)$ is the I value at time t for I_2–air(s) not passing through the contactor when the partial pressure of I_2 is P_{in}, and P_{in} is the partial pressure of I_2 in I_2–air(s) corresponding to the peak height of the rectangular input pulse. P_{in} is calculated from the partial pressure of I_2 in I_2–air(o), P_{in-o}, using

$$P_{in} = \frac{F_s}{F_s + F_3 + F_4 + F_5} \times P_{in-o} \quad (4)$$

where F_s is the flow rate of I_2–air(o) from the syringe pump and F_3, F_4, and F_5 are the flow rates of CO_2–air, air, and humidified air, respectively, from the mass-flow controllers (Fig. 1; Table S1†). As shown in Section S1.2 in the ESI,† P_{in-o} was experimentally determined to be 7.1 ± 0.2 Pa on the basis of ion chromatography analysis of I^- and IO_3^- in 20 mM NaOH solutions that had captured I_2 from I_2–air(o). Letting P_0 be the value of P_{in} in our experiments, when 12.5 mL of I_2–air(o) was injected in 300 s at a flow rate F_s of 4.17×10^{-5} dm³ s⁻¹, P_0 was 41 mPa, yielding a concentration of 0.40 ppmv.

For the clay sample, eight measurements of I_2 in I_2–air(s) passing through the contactor were typically made for the same sample, when the value of P_{in} was set at P_0 for the first, third, fifth, and seventh measurements and at $0.5P_0$ for the second, fourth, sixth, and eighth measurements. For the aqueous solutions, two measurements were made for the same sample with the value of P_{in} set at P_0. The input pulse width of I_2–air(s) was 300 s for all the measurements. In each measurement, the pulse was injected into the contactor at 89 s after the acquisitions on IBBCEAS started. The value of I_0 in eqn (2) and (3) was taken as the average of 10 spectra recorded 7–47 s before injecting I_2–air(s) into the contactor. Calibration pulses of I_2–air(s) not passing through the contactor were measured with the

1044 | Environ. Sci.: Atmos., 2022, **2**, 1041–1059

© 2022 The Author(s). Published by the Royal Society of Chemistry

input pulse height set at P_0, $0.8P_0$, $0.6P_0$, or $0.5P_0$ before each series and P_0 or $0.5P_0$ after each series.

The absorption spectra of I_2 at the wavelength range of 500–550 nm had both gradual absorption and strongly varying absorption and the latter was used to determine $P_{out}(t)$. The $(I_0/I_{in}(t) - 1)$ spectrum was fitted by a polynomial of order 19.[28] This smooth function was subtracted to yield a strongly varying residual spectrum: an illustrative example is shown in Fig. S2.† After the spectra of both $(I_0/I_{in}(t) - 1)$ and $(I_0/I_{out}(t) - 1)$ had been given this treatment, a principal component regression was applied to the residual spectra from $(I_0/I_{out}(t) - 1)$ to obtain a time series of I_2 concentrations while the residual spectra from $(I_0/I_{in}(t) - 1)$ were used as calibration spectra. The regression was carried out, assuming one factor, by using the FACT chemometric toolbox in Scilab software.[29,30] No H_2O absorption features were detected around 505 nm as a 6ν polyad overtone,[28] and hence the influence of water vapor was expected to be negligible (Fig. S2c†).

Returning to eqn (2), let l_{eff} represent the effective pathlength in IBBCEAS, calculated from $d_{eff}/(1 - R_m)$ (Fig. S2d†). Values of l_{eff} and R_m were approximately 600 m and 0.9997, respectively, in the wavelength range of 520–530 nm. The value of n_{I2} was taken as 28 mPa (6.9×10^{12} molecules per cm³) under the assumption that the additional flows over the mirrors (at flow rates of F7 + F8) diluted the I_2–air(s) in the detection cell, yielding a d_{eff} value of 0.20 m. The values of σ_{I2} were interpolated by using previously reported values.[31,32] The partial pressure of I_2 observed at time t, $P_m(t)$, is related to $P_{out}(t)$ based on

$$\frac{dP_m(t)}{dt} = \frac{F_{out}}{\tau_m(F_{out} + F_{add})}\{P_{out}(t) - P_{out}(t - \tau_m)\} \quad (5)$$

where F_{out} is the total flow rate at 298.2 K of I_2–air(s); F_{add} is the flow rate of air added to the IBBCEAS cell (assumed equal to F7 + F8); τ_m is the residence time of I_2 in the cell from

$$\tau_m = \frac{V_m}{F_{out} + F_{add}} \quad (6)$$

where V_m is the partial volume of the cell (6.28×10^{-2} dm³ with an effective length d_{eff} of 0.20 m). This yields a value of 6.1 s for τ_m.

2.4 Data analysis

2.4.1 residence ratios of I_2.
The residence ratio x_{out} of I_2 at time t is defined as

$$x_{out}(t) = \frac{P_{out}(t)}{P_0} \quad (7)$$

The measured residence ratio x_m of I_2 at time t is given by

$$x_m(t) = \frac{P_m(t)}{P_{0m}} \quad (8)$$

where P_{0m} is the partial pressure of I_2 for a pulse height when P_{in} is P_0:

$$P_{0m} = \frac{F_{out}}{F_{out} + F_{add}}P_0 \quad (9)$$

Substituting eqn (8) and (9) into eqn (5), we get

$$\frac{dx_m(t)}{dt} = \frac{1}{\tau_m}\{x_{out}(t) - x_{out}(t - \tau_m)\} \quad (10)$$

Values of $x_m(t)$ are approximately given by

$$x_m(t) \approx \frac{x_{out}(t) + x_{out}(t - \tau_m)}{2} \quad (11)$$

Combining eqn (10) and (11) yields

$$\frac{dx_m(t)}{dt} = \frac{2}{\tau_m}\{x_{out}(t) - x_m(t)\} \quad (12)$$

2.4.2 Rectangular input pulse signals.
Let $f_m(t)$ represent $x_m(t)$ observed in I_2–air(s) not passing through the contactor. The time series of $f_m(t)$ were nonlinearly fitted using

$$f_m(t) = a_2 + \frac{a_1 - a_2}{1 + \left(\dfrac{t}{a_3}\right)^{a_4}} \quad (0 \leq t \leq 300) \quad (13)$$

$$f_m(t) = \frac{b_1}{1 + \left(\dfrac{t - 300}{b_2}\right)^{b_3}} + b_4 \exp\{-b_5(t - 300)\} + b_6 \exp\{$$
$$-b_7(t - 300)\} + b_8 \exp\{-b_9(t - 300)\}$$
$$(t > 300) \quad (14)$$

where the parameters a_i ($i = 1$–4) and b_i ($i = 1$–9) determined from the experimental data by nonlinear regression are regulated to ensure continuity of $f_m(t)$ at 300 s as follows:

$$a_2 + \frac{a_1 - a_2}{1 + \left(\dfrac{300}{a_3}\right)^{a_4}} = b_1 + b_4 + b_6 + b_8 \quad (15)$$

If calculated values of $f_m(t)$ are less than zero, $f_m(t)$ is defined to be zero. Table S3† lists the values of a_i and b_i. As seen on the bottom row in Table S3,† the peak height of the rectangular input pulse (P_{in}) is a constant value (P_0 or $0.5P_0$) within 1% and 3%, respectively, for $P_{in} = P_0$ and $0.5P_0$ at 20–96% RH. Fig. 2 shows the time series of $f_m(t)$ curves fitted to the experimental data obtained at each RH value (see Fig. S3† for plots of the underlying data).

Unlike a previous study using the rectangular pulse method,[22] the adsorption processes examined here had a nonlinear relationship between rates and concentrations; hence, $f_m(t)$ could not be used as an input pulse in simulations to optimize parameters related to loss and adsorption of I_2 by clay samples in the contactor. Therefore, the input pulse signal in the simulation, $f(t)$, was approximated on the basis of eqn (12) using

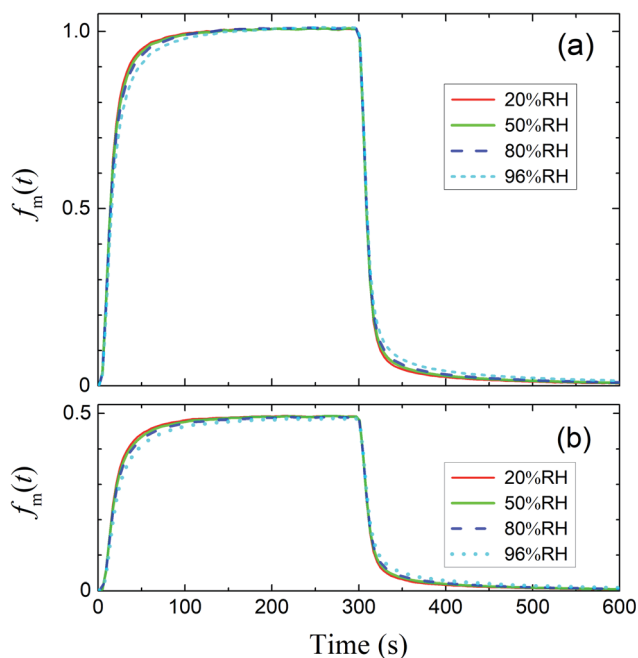$$f(t) = f_m(t) + \frac{\tau_m}{2}\frac{df_m(t)}{dt} \quad (16)$$

© 2022 The Author(s). Published by the Royal Society of Chemistry

Environ. Sci.: Atmos., 2022, **2**, 1041–1059 | **1045**

Environmental Science: Atmospheres

Paper

Fig. 2 $f_m(t)$ determined experimentally at four values of RH (a) when P_{in} is P_0 (4×10^{-7} atm) and (b) when P_{in} is $0.5P_0$ (2×10^{-7} atm).

2.4.3 First-order rate constants with respect to the concentration of gaseous I$_2$ for uptake on surfaces. The loss rate of I$_2$ by uptake on surfaces such as clay samples, $U(t)$, is calculated using

$$\frac{dP_{out}(t)}{dt} = \frac{1}{\tau_c} \times (P_0 f(t) - P_{out}(t)) - A_{np} U(t) \quad (17)$$

where $P_0 f(t)$ is the time series of I$_2$ in the input pulse, A_{np} is a unit conversion factor, and τ_c is the residence time of I$_2$–air(s) in the contactor:

$$\tau_c = \frac{V_c}{F_{out}} \frac{T_0}{T} \quad (18)$$

where V_c is the volume (3.90×10^{-1} dm^3) and T is the temperature (283.2 K) of the contactor; T_0 is 298.2 K. Eqn (17) is then rewritten as

$$U(t) = \frac{1}{A_{np}} \left\{ \frac{P_0 f(t) - P_{out}(t)}{\tau_c} - \frac{dP_{out}(t)}{dt} \right\} \quad (19)$$

From eqn (12), (16) and (19), $U(t)$ can be expressed in terms of $f_m(t)$ and $x_m(t)$, as shown in the ESI,† using

$$U(t) = \frac{P_0}{A_{np}} \times \left(\frac{f_m(t) - x_m(t)}{\tau_c} - \frac{\tau_m}{2\tau_c} \frac{dx_m(t)}{dt} + \frac{\tau_m}{2\tau_c} \frac{df_m(t)}{dt} \right.$$
$$\left. - \frac{\tau_m}{2} \frac{d^2 x_m(t)}{dt^2} - \frac{dx_m(t)}{dt} \right) \quad (20)$$

Here, values of $f_m(t)$ and $df_m(t)/dt$ were calculated from eqn (13), and values of $dx_m(t)/dt$ and $d^2 x_m(t)/dt^2$ were obtained for each value of $x_m(t)$ by quadratic curve fitting of five data points from $(t - 8)$ to $(t + 8)$. The first-order rate constant for uptake of

I$_2$ on the surface with respect to $x_{out}(t)$ at time t, $k_{1\text{-}a}(t)$, is given from eqn (12) using

$$k_{1\text{-}a}(t) = \frac{\frac{f_m(t) + \frac{\tau_m}{2} \frac{df_m(t)}{dt}}{\tau_c} - \frac{\tau_m}{2} \frac{d^2 x_m(t)}{dt^2} - \frac{dx_m(t)}{dt}}{x_m(t) + \frac{\tau_m}{2} \frac{dx_m(t)}{dt}} - \frac{1}{\tau_c} \quad (21)$$

If uptake of I$_2$ on the contactor is negligibly small, the deposition rate at time t, $k_{g\text{-}a}(t)$ in cm s^{-1}, is then

$$k_{g\text{-}a}(t) = k_{1\text{-}a}(t) \times \frac{S_c}{S} \times h_c$$
$$= \left(\frac{\frac{f_m(t) + \frac{\tau_m}{2} \frac{df_m(t)}{dt}}{\tau_c} - \frac{\tau_m}{2} \frac{d^2 x_m(t)}{dt^2} - \frac{dx_m(t)}{dt}}{x_m(t) + \frac{\tau_m}{2} \frac{dx_m(t)}{dt}} - \frac{1}{\tau_c} \right)$$
$$\times \frac{S_c}{S} \times h_c \quad (22)$$

where h_c is the height of the contactor (7.5 cm). Values of $k_{g\text{-}a}(t)$ are related not only to loss but also to adsorption of I$_2$ on the samples. The apparent surface resistance for I$_2$ above the surface, $R_{g\text{-}a}(t)$, is the reciprocal of $k_{g\text{-}a}(t)$:

$$R_{g\text{-}a}(t) = \frac{1}{k_{g\text{-}a}(t)} \quad (23)$$

2.4.4 Parameter fitting by simulations to estimate surface resistance for I$_2$. The parameters related to I$_2$ uptake on surfaces were determined by a simulation in which the parameters were fitted to reproduce the time series of $x_m(t)$ by using the parameter-fitting routine of FACSIMILE software (MCPA Software Ltd., UK).[22] It is briefly described in Section 3.

3. Results and discussion

3.1 Blank experiments

Blank experiments were run in which I$_2$–air(s) flowed through the contactor with no samples at each value of RH. These assumed perfect mixing of the gas phases and that no loss or adsorption of I$_2$ occurred in the contactor:

$$\frac{dx_{out}(t)}{dt} = \frac{1}{\tau_c} \times (f(t) - x_{out}(t)) \quad (24)$$

Here, $f(t)$ is calculated from $f_m(t)$ using eqn (16), and $x_{out}(t)$ is related to $x_m(t)$ by eqn (12).

The measured time series (Fig. 3) showed that $x_m(t)$ before and after 300 s was smaller and larger, respectively, than the dashed curve representing the simulation results, which showed that I$_2$ was reversibly adsorbed on the inner wall of the contactor. This reversible adsorption of I$_2$ increased with increasing RH.
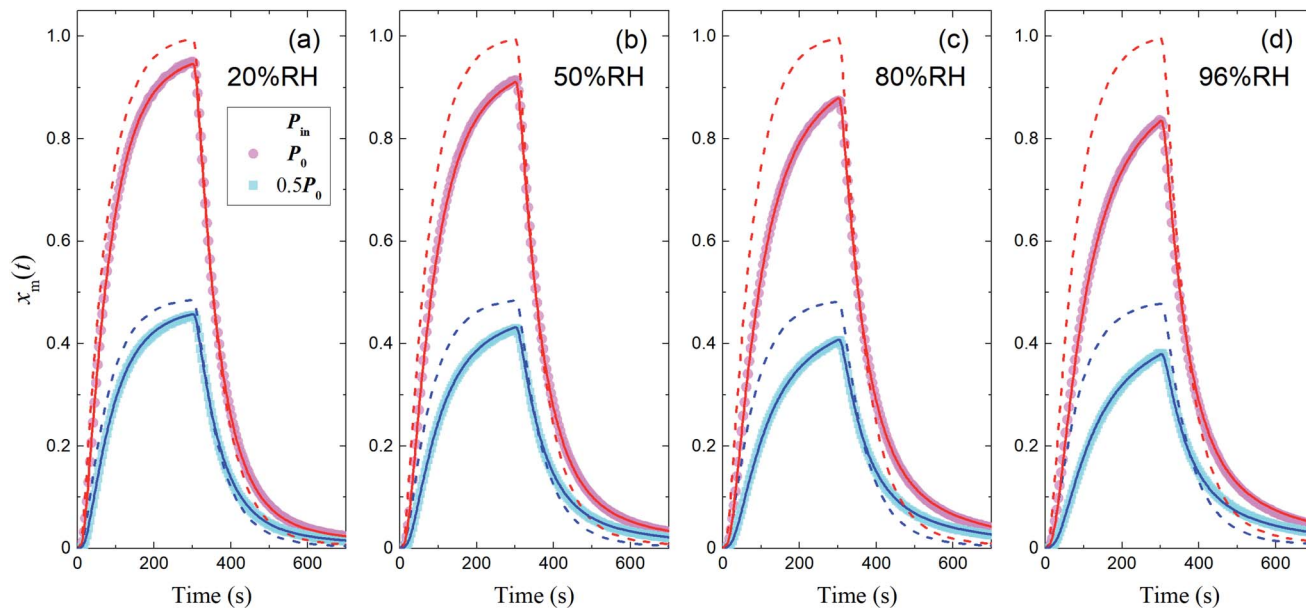
Fig. 3 Time series of $x_m(t)$ for I_2 in blank experiments at four RH values. P_{in} was P_0 (4.0×10^{-7} atm; pink circles) or $0.5P_0$ (2.0×10^{-7} atm; blue squares), the temperature was 283.2 K, and F_{out} was (a) 7.315×10^{-3}, (b) 7.281×10^{-3}, (c) 7.302×10^{-3}, and (d) 7.369×10^{-3} dm^3 s^{-1}. Dashed curves are the simulation results without loss or adsorption of I_2 (from eqn (24)) and solid curves are fitted to the experimental results using eqn (26)–(28).

The apparent uptake rates of I_2 by the contactor decreased with time, although the gas-phase concentrations of I_2 increased (Fig. S4†). This result suggests that the uptake occurred as an initial rapid stage followed by a slow stage, as documented for the sorption of volatile organic compounds on soil particles.[33] I_2 was readily adsorbed on the contactor walls, then transformed to internal surfaces, such as pores, at a slower rate. Thus our simulation assumed Freundlich-type adsorption of I_2 on the contactor walls (eqn (25)) and a reversible transformation of I_2 between the surface and internal sites:

$$y_b(t) = K_{bads}x_{out}(t)^{1/N} \tag{25}$$

where $y_b(t)$ is the amount of I_2 on the wall surface; K_{bads} and N are parameters of Freundlich adsorption equilibrium and N is 2 here, and

$$\frac{dx_{out}(t)}{dt} = \frac{1}{\tau_c} \times (f(t) - x_{out}(t)) - k_{bm} \times \left\{ x_{out}(t) - \left(\frac{y_b(t)}{K_{bads}}\right)^N \right\} \tag{26}$$

$$\frac{dy_b(t)}{dt} = A_{bpn}k_{bm} \times \left\{ x_{out}(t) - \left(\frac{y_b(t)}{K_{bads}}\right)^N \right\} - k_{bf}y_b(t) + k_{bb}z_b(t) \tag{27}$$

$$\frac{dz_b(t)}{dt} = k_{bf}y_b(t) - k_{bb}z_b(t) - k_{bl}z_b(t) \tag{28}$$

where k_{bm} is the mass-transfer coefficient of I_2 between the gas phase and the wall surface; k_{bf} and k_{bb} are first-order forward and backward rate constants, respectively, for the transport of adsorbents between surface and internal sites in the wall; k_{bl} is

a first-order rate constant for I_2 loss in the internal sites; $z_b(t)$ is the amount of I_2 in the internal sites; and A_{bpn} is a unit conversion factor. Simulations using eqn (12) and eqn (26)–(28) were conducted to simultaneously reproduce the observed time series of $x_m(t)$ with values of K_{bads}, k_{bf}, k_{bb}, and k_{bl} as common parameters for each value of RH while a value of k_{bm} is a common parameter for all data.

The solid curves in Fig. 3 show $x_m(t)$ values from the simulation that minimized the residual sum of squares (RSS); the observed data were satisfactorily reproduced. The values determined for each parameter are listed in Table S4,† which also lists mole ratios of I_2 loss. In the blank experiments, the loss ratio of I_2 increased from 2.7% to 12.6% with increasing RH for P_0 as P_{in} and from 2.2% to 15.6% for $0.5P_0$ as P_{in}. Langmuir-type adsorption of I_2 on the contactor also reproduced the $x_m(t)$ time series (Table S5†), but the Freundlich-type equation fitted the data with a smaller RSS, as shown in the ESI.† The parameters determined at each RH value (Table S4†) were used to estimate $k_{1\text{-}a}(t)$ and simulate $x_m(t)$ in the other experiments.

3.2 Uptake of I_2 by aqueous solutions

In the time series of $x_m(t)$ in I_2–air(s) after passage through the contactor with dishes holding 2.8 mL of water, 1 mM aqueous sulfuric acid, or 1 mM or 10 mM aqueous ascorbic acid in small basins (S/S_c, 0.138), maximum values of $x_m(t)$ for water and sulfuric acid were both ~5% smaller than those of the blank, and values for ascorbic acid were ~40% smaller than those of the blank (Fig. 4). The similar time series for water and sulfuric acid suggests that the water surface was saturated with undissociated I_2 under the experimental conditions such that the uptake of I_2 was controlled by aqueous-phase diffusion of I_2.
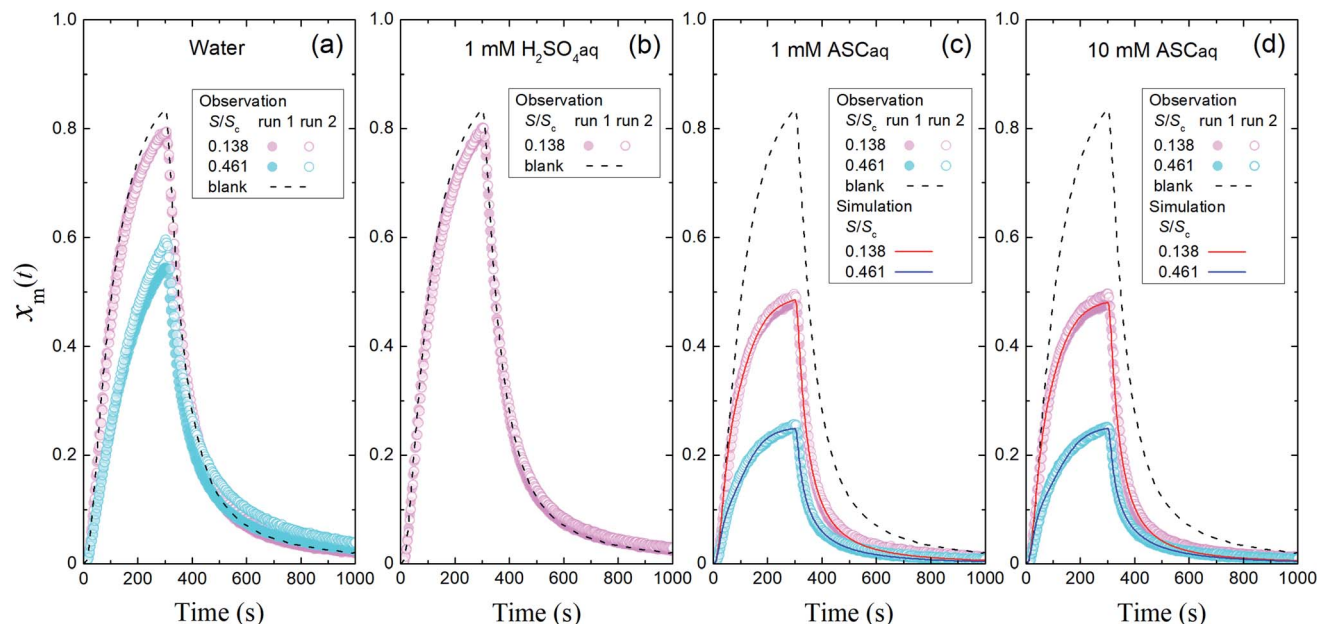
© 2022 The Author(s). Published by the Royal Society of Chemistry

Environ. Sci.: Atmos., 2022, **2**, 1041–1059 | **1047**

Fig. 4 Time series of $x_m(t)$ in I_2–air(s) (P_{in}, 4.0×10^{-7} atm) after passage through the contactor over (a) water, (b) 1 mM aqueous sulfuric acid (H_2SO_4aq), (c) 1 mM aqueous ascorbic acid (ASCaq), and (d) 10 mM ASCaq. Blank runs are shown as dashed curves. Pink symbols are the results for 2.8 mL of solution in the small basin (S/S_c, 0.137) of the contactor dish, and blue symbols are the results for 9.4 mL of solution in the large basin (S/S_c, 0.461). The red and blue curves are the simulation results obtained by using eqn (S11)–(S13).†

The dissociation ratio in reaction (R1) was estimated at 16% under the experimental conditions (283 K; pH, 5.6 for water in equilibrium with 400 ppmv CO_2; partial pressure of I_2, 3.2×10^{-7} atm) according to

$$\frac{[HOI]}{[I_2]} = \frac{[I^-]}{[I_2]} = \sqrt{\frac{K_a}{K_H P_{I_2} [H^+]}} \quad (29)$$

where K_a is the dissociation constant of reaction (R1) at 283 K, K_H is the Henry's law constant of I_2 at 283 K, and P_{I2} is the partial pressure of I_2 (see the ESI†). In contrast, in ascorbic acid, I_2 was reduced to I^- based on

$$I_2 + C_6H_8O_6 \rightarrow 2H^+ + 2I^- + C_6H_6O_6 \quad (R3)$$
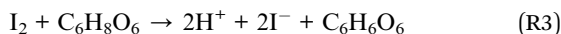
and I_2 uptake proceeded much faster than in water. With the reported rate constant for reaction (R3) of 1.2×10^5 M^{-1} s^{-1} at 20 °C,[34] the lifetime of I_2 with respect to reaction (R3) in 10 mM ascorbic acid is estimated at about 10^{-3} s at 20 °C, which is two orders of magnitude shorter than that of I_2 with respect to hydrolysis in reaction (R1).[35] In this solution, I_2 thus reacts dominantly with ascorbic acid. However, the similar time series of $x_m(t)$ for 1 mM and 10 mM ascorbic acid (Fig. 4c and d) suggests that the rate-limiting step is not the aqueous reaction but mass transfer in the gas-film layer, as described by two-film layer theory. We estimated the resistance for I_2 for mass transfer in the gas-film layer above ascorbic acid, or $R_{g-cont-w}$, under the experimental conditions from the $k_{1-a}(t)$ values and simulations for 10 mM ascorbic acid, and as discussed below, we were able to compare them with the corresponding uptake coefficients (γ) of I_2 estimated from previously published data.

Fig. 4 also shows the time series of $x_m(t)$ for experiments with 9.4 mL of liquid in the contactor dish with a large basin (S/S_c, 0.461). Loss rates of I_2 through uptake on the surface, $U(t)$, were calculated during the injection period (13–289 s) using eqn (20). After 50 s, these values decreased with time for water and the blank but were almost constant for 10 mM ascorbic acid (Fig. 5a). Because the gas-phase concentration of I_2 increased with time, the rate constants $k_{1-a}(t)$ calculated using eqn (21) decreased with time (Fig. 5b). The $k_{1-a}(t)$ value for uptake by the contactor (Table S6†) was subtracted from the rate constants, and the remainders were used to calculate deposition rates, $k_{g-a}(t)$, using eqn (22) (Fig. 5c).

The rate constant k_{1-a} and the deposition rate k_{g-a} were defined as the average of 10 data points of $k_{1-a}(t)$ and $k_{g-a}(t)$, respectively, from 253–289 s and the surface resistance R_{g-a} was determined to be the reciprocal of k_{g-a}. When the $k_{1-a}(t)$ value for the blank with P_0 as P_{in} was subtracted from the rate constants in the first experimental run, the k_{g-a} values in 10 mM ascorbic acid were 0.91 ± 0.03 cm s^{-1} for the small basin and 0.85 ± 0.01 cm s^{-1} for the large basin, yielding R_{g-a} values of 109 s m^{-1} and 118 s m^{-1}, respectively. Values of k_{1-a}, k_{g-a}, and R_{g-a} were estimated similarly for all of the aqueous solutions (Table S6†).

Simulations were carried out to distinguish the uptake of I_2 by ascorbic acid and the contactor (Section S6-3 in the ESI†). Letting k_m be the mass-transfer coefficient of I_2 in the gas-film layer above ascorbic acid, values of k_m are thus estimated to be 0.91 ± 0.01 cm s^{-1} and 0.78 ± 0.01 cm s^{-1} for the small and large basins, respectively (errors at 90% confidence level). These values are approximately equal to the estimated values of k_{g-a}. Overall, R_g is estimated to be 120 ± 5 s m^{-1} from 16 data of R_g-

1048 | *Environ. Sci.: Atmos.*, 2022, **2**, 1041–1059

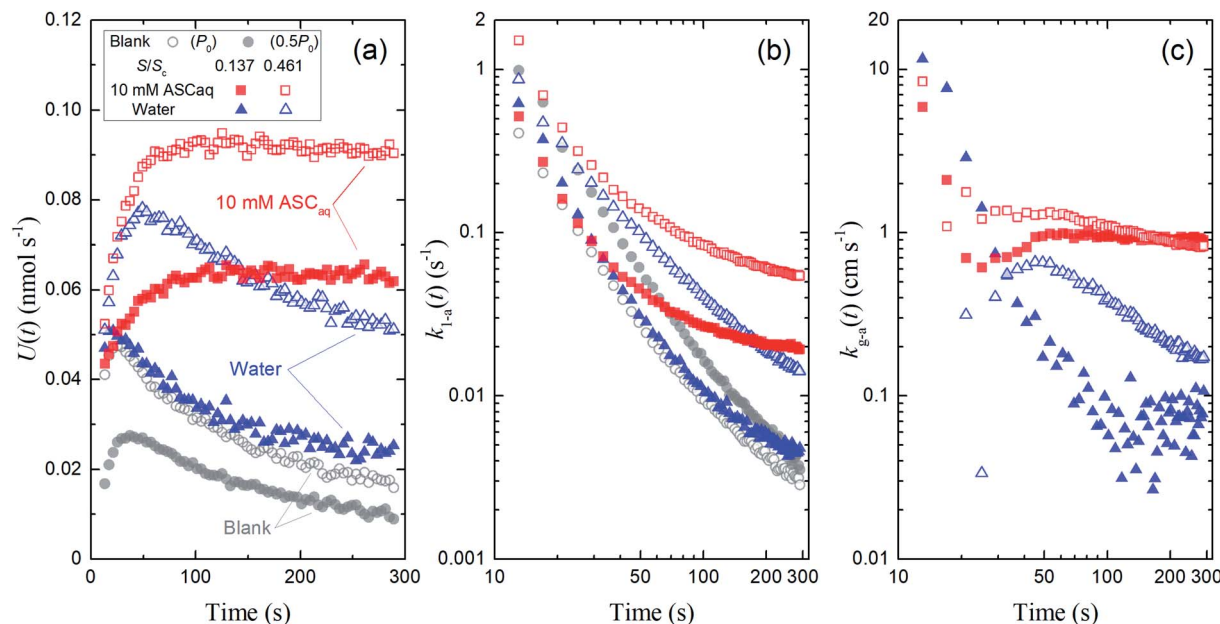© 2022 The Author(s). Published by the Royal Society of Chemistry

Fig. 5 Time series of (a) loss rates of I_2 by uptake on surfaces, $U(t)$, (b) their apparent first-order rate constants, $k_{1-a}(t)$, and (c) their apparent deposition rates, $k_{g-a}(t)$ in blanks and the first experimental run for 10 mM ascorbic acid and water in small basins ($S/S_c = 0.138$, closed symbols) and large basins ($S/S_c = 0.461$; open symbols). Red square symbols represent the results for ascorbic acid, blue triangle symbols represent the results for water, and gray circle symbols represent the results for blank (open circles, P_0 as P_{in} at 96% RH; closed circles, $0.5P_0$ as P_{in} at 96% RH; the former was taken as the blank to obtain $k_{g-a}(t)$ values here).

$_a$ for 1 mM and 10 mM ascorbic acid (Table S6†). Errors represent the standard deviation.

Referring to the reported physicochemical properties of I_2,[34,36–38] we estimate the uptake coefficients (γ) of I_2 at 2.6×10^{-3} for 10 mM ascorbic acid and 1.0×10^{-3} for 1 mM ascorbic acid (Section S6.4. in the ESI†). In this estimate, 10^{-2} was adopted as the accommodation coefficient of I_2.[36] In the absence of the gas-film transfer limitation, the R_g values for I_2 above ascorbic acid would be 10 s m^{-1} and 26 s m^{-1}, respectively (the ESI†). These values are much smaller than the R_g values obtained here; this supports our experimental finding that the R_g value of 120 s m^{-1} is the resistance for mass transfer of I_2 in the gas-film layer above aqueous surfaces ($R_{g-cont-w}$). This value of $R_{g-cont-w}$ was used as the resistance for mass transfer of I_2 in the gas-film layer above clay samples in Section 3.3.

Fig. 4 and 5 suggest that uptake of I_2 by water differed with basin size, probably because of a difference in aqueous-phase turbulence between them. We did not obtain surface resistance for I_2 above water. As seen in eqn (29), dissociation of I_2 in water occurs much more strongly in the atmosphere than that observed here because the partial pressure of I_2 is very low, and I_2 uptake on aqueous surfaces in the atmosphere is determined not only by turbulence near surface water but also by hydrolysis in reaction (R1).[36] For ascorbic acid, because the leaf apoplast contains ascorbic acid, reaction (R3) is expected to proceed in the leaf interior, where O_3 is taken up by ascorbic acid.[39] However, this will happen only in the small number of plants that open their stomata at night.[19]

3.3 Uptake by clay samples

3.3.1 Loss and adsorption ratios of I_2. The first of our experiments with a flow of I_2–air(s) over the clay samples was conducted at 80% RH and yielded $x_m(t)$ values that were definitely smaller than those of the blank experiment (Fig. 6). For each clay sample, $x_m(t)$ was smaller in the large basins than in the small basins. These results showed that I_2 was deposited on the clay samples and removed from the gas phase. Uptake of I_2 by clay samples probably involved irreversible adsorption of I_2 in micropores of clay minerals because of the relatively large size of I_2, as reported for I_2 uptake by active carbons.[40] This decrease of $x_m(t)$ varied among the clay samples, but the variation was small compared to that of the BET surface areas of the samples (Table 1). Fig. S5 and S6† show the results for 20% RH and 50% RH, respectively.

Loss ratios of I_2 were defined as $\Delta Q_{loss}/Q_{in}$, where $\Delta Q_{loss} = Q_{in} - Q_{out}$, Q_{in} was the amount of I_2 entering the contactor, and Q_{out} was the integrated amount of I_2 observed at 0–1709 s in I_2–air(s) leaving the contactor. Loss ratios of I_2 decreased over successive runs for every clay sample. The decrease was greatest after run 1 (Fig. 7). Loss ratios decreased with increasing RH from 20% RH to 80% RH for all runs of allophane and for runs 3–7 of illite and kaolinite. This dependence on RH tended to strengthen as runs were repeated. Loss ratios for montmorillonite, halloysite, and AgroMAT AG-1 decreased between 20% RH and 50% RH and increased between 50% RH and 80% RH. However, the latter increase was also evident in the blank experiments. This relative-humidity dependence is discussed in Section 3.3.3 (see eqn (40)).
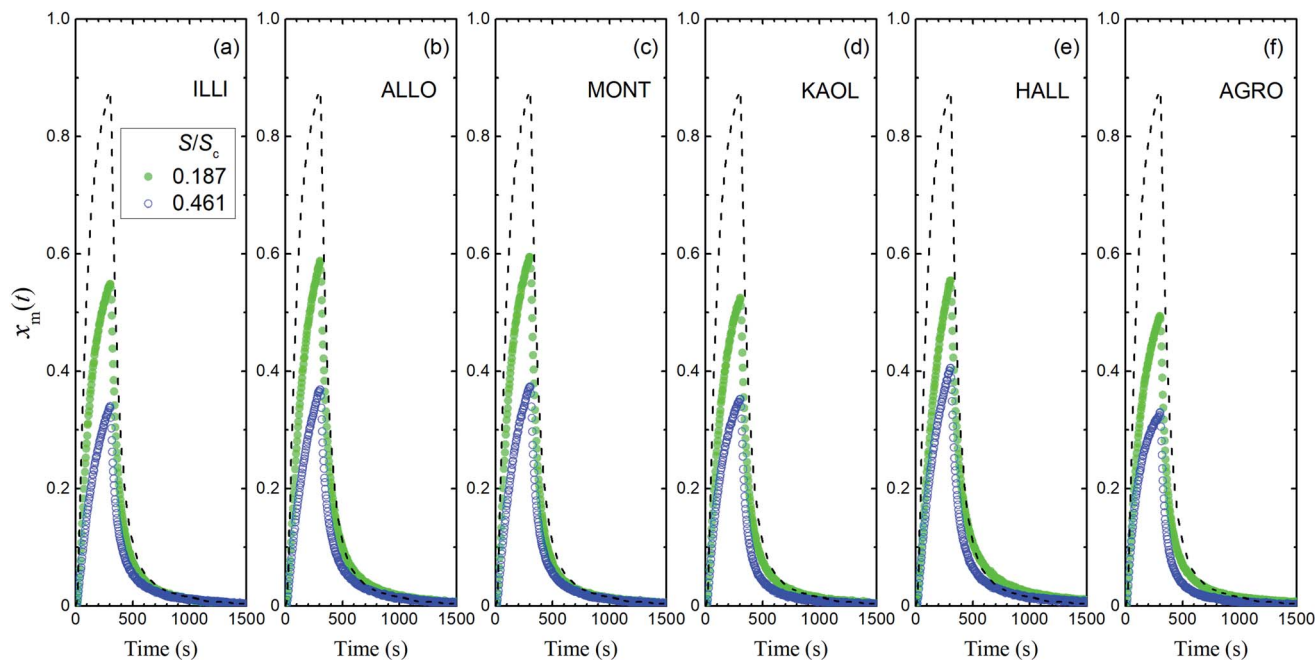
© 2022 The Author(s). Published by the Royal Society of Chemistry

Environ. Sci.: Atmos., 2022, **2**, 1041–1059 | **1049**

Fig. 6 Time series of $x_m(t)$ in I_2–air(s) (P_{in}, 4.0×10^{-7} atm) after passage through a contactor containing (a) illite, (b) allophane, (c) montmorillonite, (d) kaolinite, (e) halloysite, or (f) AgroMAT AG-1 in run 1 at 80% RH in small basins (S/S_c, 0.187; sample, 0.73 g; green closed symbols) and large basins (S/S_c, 0.461; sample, 1.78 g; blue open symbols). Dashed curves show time series of $x_m(t)$ in blank experiments at 80% RH.
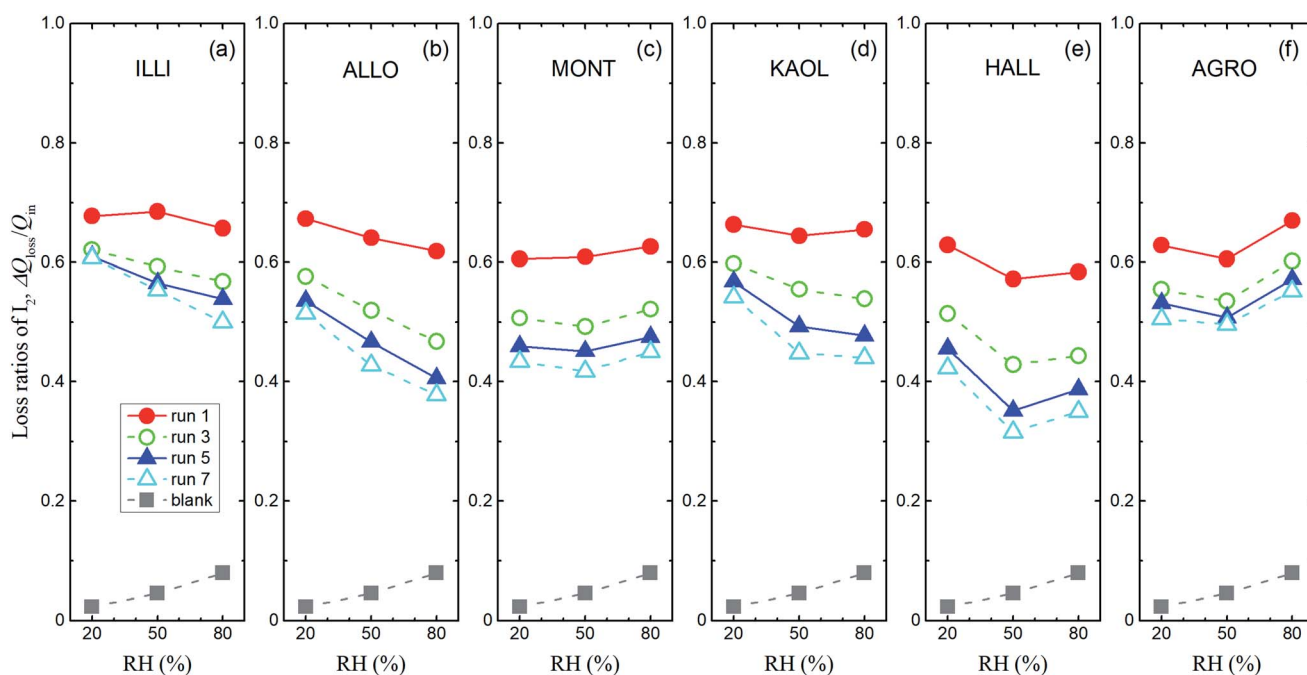

Fig. 7 Loss ratios of I_2, $\Delta Q_{loss}/Q_{in}$ versus RH for I_2–air(s) mixtures flowing over large basins of (a) illite, (b) allophane, (c) montmorillonite, (d) kaolinite, (e) halloysite, and (f) AgroMAT AG-1 samples in odd-numbered runs (P_{in}, 4.0×10^{-7} atm). Gray squares show $\Delta Q_{loss}/Q_{in}$ in blank experiments with P_0 as P_{in}.

Fig. 8 shows the time series of $x_m(t)$ in odd-numbered runs for kaolinite at 80% RH along with the same profiles normalized to the maximum (x_{m-max}) in each run to bring out changes in the profile shape with successive runs. The monotonic decrease

with successive runs of the ratios of the integrated amount of I_2 during the injection period (0–300 s) to that after 300 s meant that there was an increase in the ratio of I_2 adsorption to I_2 loss. Fig. 9 shows stacked column charts of $\Delta Q_{loss}/Q_{in}$ and $\Delta Q_{ads}/Q_{in}$
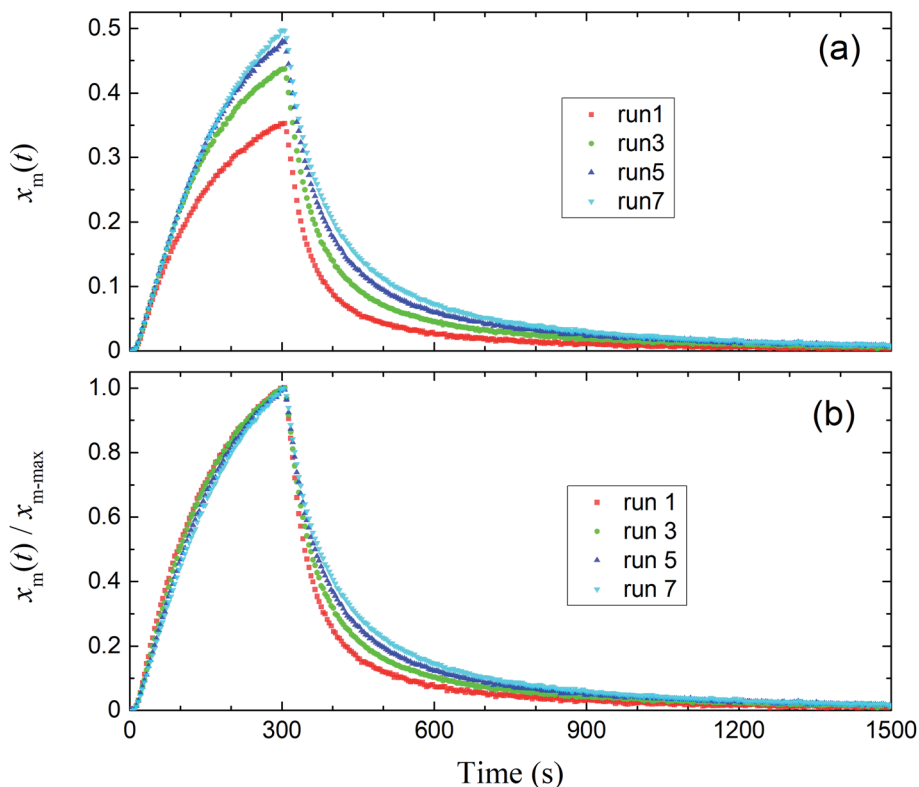
Fig. 8 (a) Time series of $x_m(t)$ in I_2–air(s) for odd-numbered runs with kaolinite in the small basin at 80% RH (P_{in}, 4.0×10^{-7} atm). (b) Normalized time series from (a).

for odd-numbered runs with each clay sample at 80% RH. ΔQ_{ads} is the amount of I_2 reversibly adsorbed on the clay samples and was defined as $\Delta Q_{ads} = Q_{aft} - Q_{300} - Q_{saft}$ where Q_{aft} is the integrated amount of I_2 observed at 301–1709 s in I_2–air(s) leaving the contactor, Q_{300} is the amount of gaseous I_2 in the contactor at 300 s, and Q_{saft} is the integrated amount of I_2 in I_2–air(s) entering the contactor at 301–1709 s (Fig. 2). ΔQ_{loss} decreased and ΔQ_{ads} increased with successive runs; the sum of ΔQ_{loss} and ΔQ_{ads}, which represented the amount of I_2 accommodated by clay samples, remained almost constant or decreased more slowly than ΔQ_{loss} with successive runs. This behavior could be explained by using a two-stage model with two kinds of active sites on the surface and in the interior for loss of I_2. One kind was consumed on the surface, and the other retained its activity in the interior for uptake of I_2, as shown in Section 3.3.3. Similar behavior of $\Delta Q_{loss}/Q_{in}$ and $\Delta Q_{ads}/Q_{in}$ over successive runs was observed at 20% RH and 50% RH and for even-numbered runs (Fig. S7–S11†).

3.3.2 Apparent surface resistance for I_2. We calculated I_2 loss rates through surface uptake $U(t)$, the rate constants $k_{1\text{-}a}(t)$, and the deposition rates $k_{g\text{-}a}(t)$ during the injection period (13–289 s) for each run of the clay experiments at the two basin sizes. Fig. 10 shows the results of runs 1 and 5 with illite at 80% RH. We then used a procedure analogous to our procedure for the aqueous solutions (Section 3.2) to obtain the apparent surface resistance, $R_{g\text{-}a}$, above the clay samples (Tables S8–S13) as described in Section S7.3 in the ESI.†

If $R_{g\text{-cont}}$ is the resistance for mass transfer of I_2 in the gas-film layer above clay samples in the contactor, the surface resistance for I_2 above clay samples, $R_{g\text{-}a\text{-clay}}$, is given by

$$R_{g\text{-}a\text{-clay}} = R_{g\text{-}a} - R_{g\text{-cont}} \tag{30}$$

The $R_{g\text{-cont-w}}$ value above ascorbic acid (120 ± 5 s m^{-1}; Section 3.2) was taken as the value of $R_{g\text{-cont}}$ in eqn (30). Fig. 11 shows the $R_{g\text{-}a\text{-clay}}$ values thus calculated from the average of $R_{g\text{-}a}$ values for each clay sample with the $R_{g\text{-cont-w}}$ value.

However, as is apparent in Tables S8–S13,† the values of $R_{g\text{-}a}$ for all clay samples in even-numbered runs (P_{in}, $0.5P_0$) are apparently smaller than the $R_{g\text{-}a}$ values in odd-numbered runs (P_{in}, P_0), except for run 1. This pattern suggests that there was a systematic error in the determination of $R_{g\text{-}a}$. This error was probably caused by the fact that the degree of decrease in $k_{1\text{-}a}(t)$ with time differed between even-numbered and odd-numbered runs because the values of P_{in} differed and because the differences varied between each run and blank. To reduce these errors, the mass-transfer processes of I_2 in a gas-film layer above clay samples need to be formulated and then taken into account in a simulated calculation to reproduce the decrease of I_2 uptake rates with time and to distinguish between I_2 uptake on clay samples and uptake on the wall surfaces of the contactor (blank). The parameters obtained in the simulation were used to estimate I_2 uptake rates at the low concentrations of I_2 that might be found in the atmosphere.
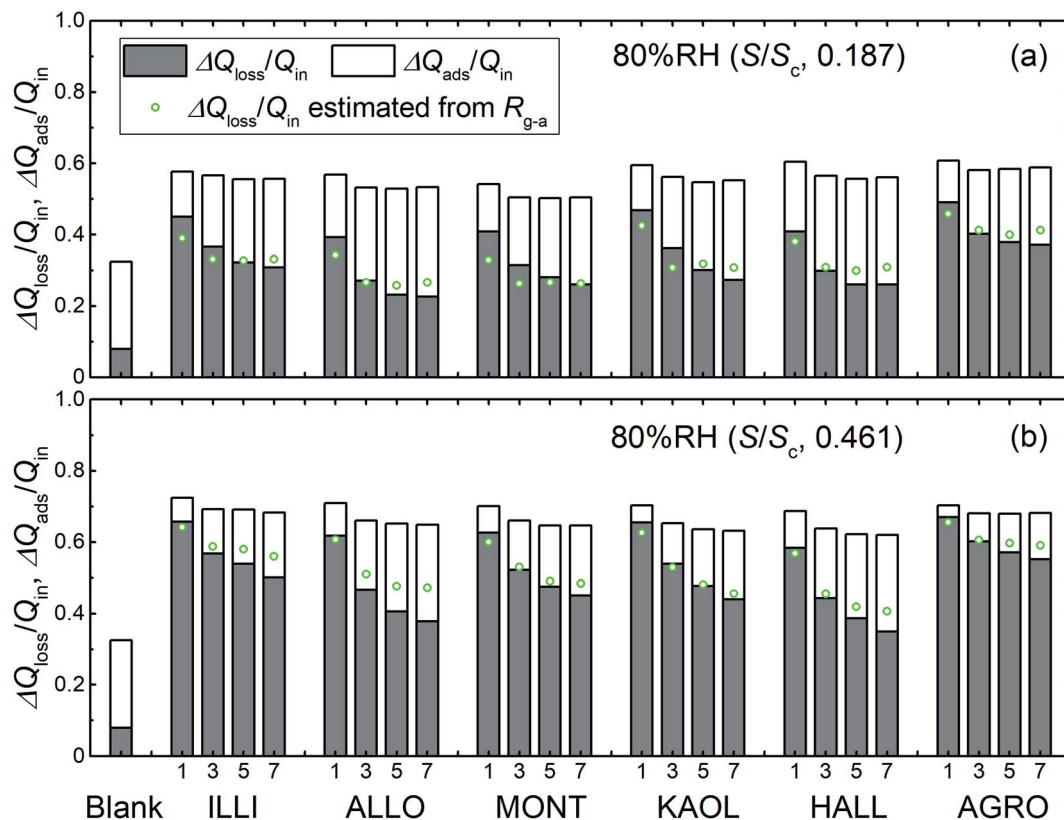
© 2022 The Author(s). Published by the Royal Society of Chemistry

Environ. Sci.: Atmos., 2022, **2**, 1041–1059 | **1051**

Fig. 9 Loss ratios ($\Delta Q_{loss}/Q_{in}$, grey columns) and adsorption ratios ($\Delta Q_{ads}/Q_{in}$, white columns) of I$_2$ for blank and odd-numbered runs with each clay sample, (a) in small basins (S/S_c, 0.187) and (b) in large basins (S/S_c, 0.461), at 80% RH (P_{in}, 4.0×10^{-7} atm). Green circles represent loss ratios, $\Delta Q_{loss}/Q_{in}$, calculated from R_{g-a} (Tables S8–S13†) with eqn (S21).†

3.3.3 Simulation of I$_2$ uptake by clay samples.

The simulation was conducted on the basis of a two-stage model in which the uptake of I$_2$ by clay samples occurred *via* an initial stage of rapid sorption onto surface sites followed by a stage of slow sorption onto interior sites such as the mesopores and the micropores of clay samples. Such a two-stage process has been documented for the sorption of volatile organic compounds on soil particles.[33] Kinetics of adsorption on porous solids such as clay particles in the gas phase and in liquid phase has been investigated on the basis of intraparticle diffusion models or surface reaction models.[33,41,42] Statistical rate theory also approached adsorption/desorption kinetics for homogeneous and heterogeneous solid surfaces.[41] We used a surface reaction model assuming homogeneous surfaces. This model was simple but could reproduce the time series of $x_m(t)$ in consecutive runs as shown below.

For the first stage, as mentioned in the previous section, we assumed that the mass-transfer rates of the I$_2$ in the gas-film layer above the clay samples were represented by a time-dependent function of $k_m(t)$ that took positive values for the mass transfer from the gas to surfaces and negative values for the reverse transfer. This scenario is analogous to a model for gas-film layer diffusion followed by Langmuir-type adsorption (see the ESI†) and takes the form

$$\frac{dx_{out}(t)}{dt} = \frac{1}{\tau_c} \times (f(t) - x_{out}(t)) - \frac{S}{S_c h_c} k_m(t) \times x_{out}(t) - k_{bm}$$
$$\times \left\{ x_{out}(t) - \left(\frac{y_b(t)}{K_{bads}}\right)^2 \right\} \quad (31)$$

$$k_m(t) = k_{ma} \times \frac{x_{out}(t) - \frac{\theta(t)}{1-\theta(t)}\frac{1}{K_{ads}}}{x_{out}(t)} \quad (32)$$

where K_{ads} is the equilibrium coefficient for the adsorption of I$_2$ onto clay samples, and k_{ma} is a parameter needed to determine $k_m(t)$; it is noteworthy that k_{ma} may take larger values than the actual mass-transfer rates of I$_2$ in the gas-film layer. Here, $\theta(t)$ is the fractional coverage on the surface, that is, q_t/q_∞, where q_t and q_∞ denote the amount of I$_2$ adsorbed at time t and when the clay surface is fully saturated, respectively.

For the second stage, some of the adsorbed I$_2$ is assumed to transfer between the surface and the interior sites and some is lost. As described in Section 3.3.1, the loss ratios of I$_2$ decreased over successive runs for every clay sample. The decrease was greatest after run 1 and remained finite through each set of experimental runs. This pattern suggests different kinds of active sites for loss of I$_2$. We hence assumed that there were two kinds of active sites: one kind was consumed on the surface, and the other retained its activity in the interior for uptake of I$_2$ as follows:
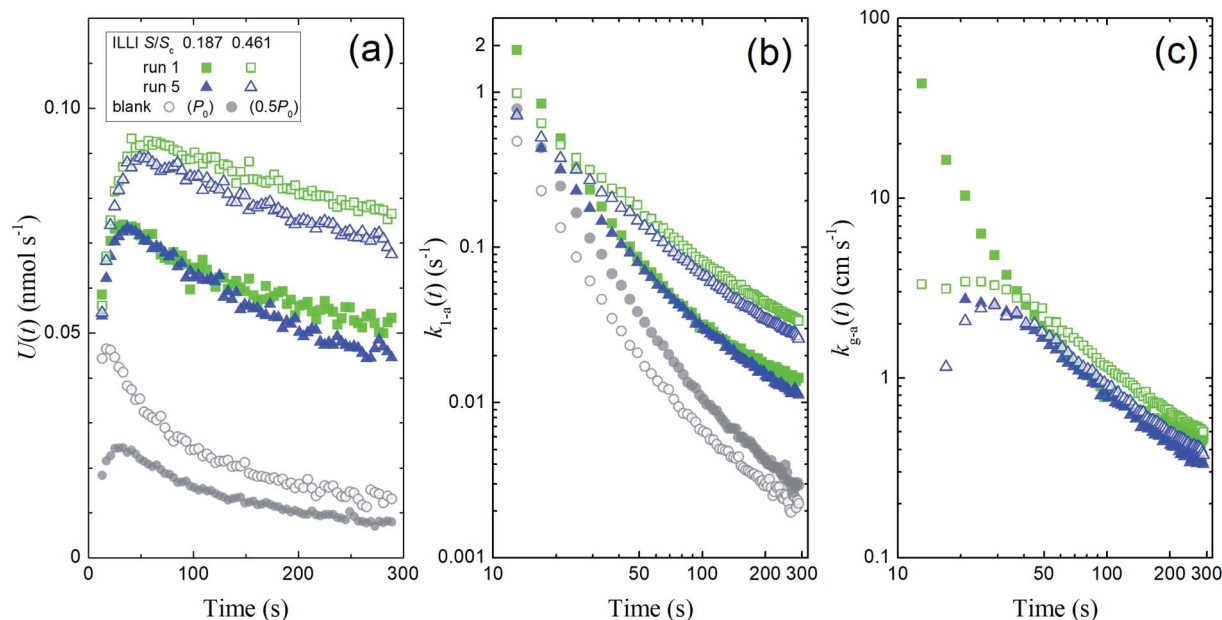
Fig. 10 Plots calculated from the experimental results during I_2 injection over illite at 80% RH showing (a) loss rates of I_2 by surface uptake, $U(t)$, (b) the apparent first-order rate constants $k_{1\text{-a}}(t)$, and (c) the apparent deposition rates $k_{\text{g-a}}(t)$ in blank experiments and in runs 1 and 5 with small basins (S/S_c, 0.187; closed symbols) and large basins (S/S_c, 0.461; open symbols). Green squares indicate the results in run 1, blue triangles indicate the results in run 5, and grey circles indicate the results for the blank run (open circles, $P_{\text{in}} = P_0$; closed circles, $P_{\text{in}} = 0.5P_0$). The $k_{1\text{-a}}(t)$ value for the blank with $P_{\text{in}} = 0.5P_0$ was subtracted from each value of $k_{1\text{-a}}(t)$, and the difference was used to calculate the $k_{\text{g-a}}(t)$ value.

$$\frac{d\theta(t)}{dt} = \frac{B_{\text{pn}}}{q_\infty} \times k_{\text{m}}(t) \times \left(x_{\text{out}}(t) - \frac{\theta(t)}{1 - \theta(t)} \frac{1}{K_{\text{ads}}} \right) - k_{\text{f}}$$
$$\times \left(\theta(t) - \frac{\varphi(t)}{K_{\text{pads}}} \right) - k_{\text{loss-s}}(t)\theta(t) \quad (33)$$

$$\frac{d\varphi(t)}{dt} = k_{\text{f}} \times \left(\theta(t) - \frac{\varphi(t)}{K_{\text{pads}}} \right) - k_{\text{loss-p}}\varphi(t) \quad (34)$$

where k_{f} is the first-order rate constant for the transfer of adsorbents from the surface to the interior sites of the clay samples, K_{pads} is the equilibrium constant of I_2 between the surface and the interior, $\varphi(t)$ is the number of the interior sites into which I_2 has been transformed as a fraction of q_∞, B_{pn} is a conversion factor used to convert units, $k_{\text{loss-p}}$ is the first-order rate constant for loss of I_2 in the interior sites that retain their activity regardless of I_2 loss. Here, $k_{\text{loss-s}}(t)$ is the time-dependent, first-order rate constant for loss of I_2 in the surface sites and is represented by

$$k_{\text{loss-s}}(t) = k_{\text{ls0}} \times \frac{n_{\text{ls}}(t)}{N_{\text{ls0}}} \quad (35)$$

where k_{ls0} is the first-order rate constant for I_2 loss for fresh clay samples at the active sites that are lost per loss of I_2, and N_{ls0} and $n_{\text{ls}}(t)$ are the numbers of these active sites as a fraction of q_∞ for fresh clay samples and for clay samples exposed to I_2–air(s) during time t, respectively. Assuming that the decrease of $n_{\text{ls}}(t)$ is equal to the loss of I_2, it follows that

$$\frac{dn_{\text{ls}}(t)}{dt} = -k_{\text{ls0}} \times \frac{n_{\text{ls}}(t)}{N_{\text{ls0}}}\theta(t) \quad (36)$$

Simulations using eqn (31)–(36) together with eqn (12), (27) and (28) were conducted to simultaneously reproduce the time series of $x_{\text{m}}(t)$ for runs 1–5 for the same clay sample in two experimental sets, one set with small basins and another with large basins for each clay sample (Fig. S12–S17†). The simulation was conducted with common values of the parameters k_{ma}, K_{ads}, k_{f}, $k_{\text{loss-p}}$, k_{ls0}, and N_{ls0} for both experimental sets and with a parameter q_∞ that varied between the sets. Fig. 12 shows the result for montmorillonite samples at 80% RH. The observed time-series of $x_{\text{m}}(t)$ were reproduced by the simulation. The active sites for I_2 loss on the surface decreased with successive runs and almost all sites were lost at the end of run 5. The observed data were similarly reproduced by the simulation for all clay samples (Fig. S12–S17†). The values of the parameters obtained in the simulation are listed in Table S14.† The residual sums of squares, RSS, for allophane and kaolinite samples at 20% RH were larger than those for the other samples. Values of k_{f} decreased with increasing relative humidity for all clay samples (Table S14†). This decrease was consistent with the scenario that a water film formed in the interior, which increased with relative humidity and decreased surface areas in shale clay,[43] reduced rates for the transfer of I_2 between the surface and the interior of clay samples.

The corresponding equilibrium constant, K_{pads}, decreased with increasing RH between 50% and 80% for illite, allophane, and kaolinite samples while it increased or remained almost constant for montmorillonite, halloysite, and AgroMAT AG-1 samples. It suggested that the water film might destabilize I_2 on the surface and in the interior to almost the same extent for the latter three clay samples since K_{pads} was the equilibrium
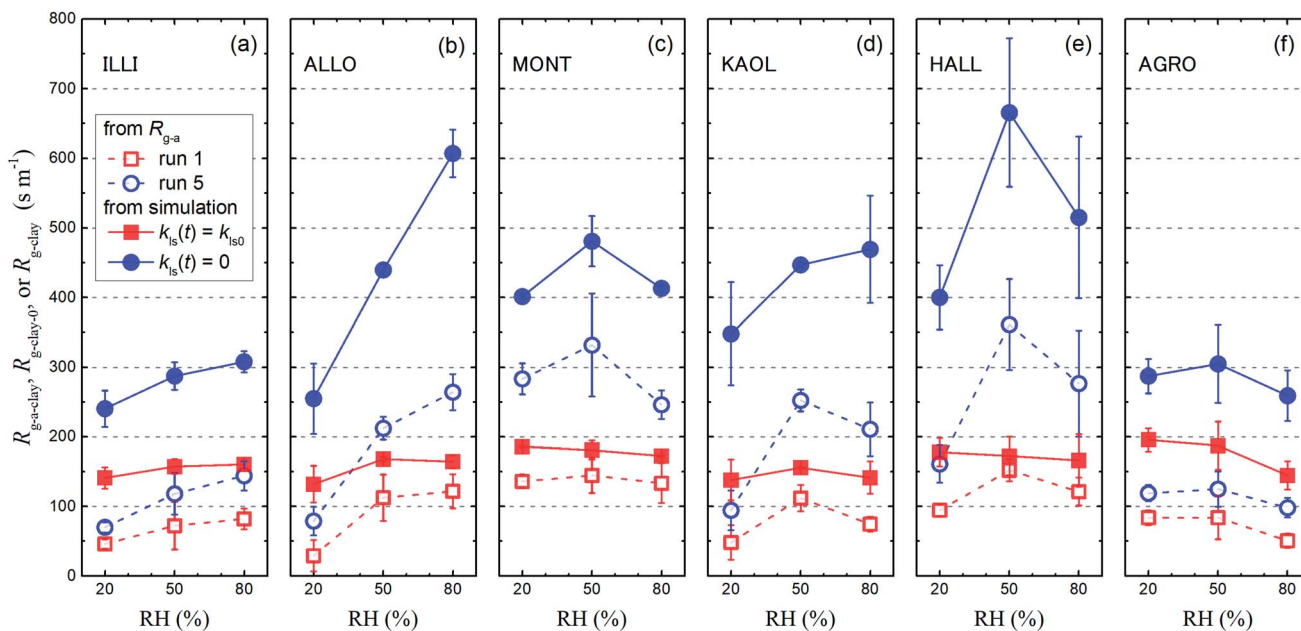
Fig. 11 Resistance for I_2 above clay samples of $R_{g\text{-a-clay}}$, $R_{g\text{-clay-0}}$, and $R_{g\text{-clay}}$ at 20% RH, 50% RH, and 80% RH. The $R_{g\text{-a-clay}}$ values (open symbols) were calculated with eqn (30) by subtracting the $R_{g\text{-cont-w}}$ value (120 s m^{-1}) from the average of the $R_{g\text{-a}}$ values with small and large basins for each clay sample in run 1 (red squares) and run 5 (blue circles) (Tables S8–S13†). Values of $R_{g\text{-clay-0}}$ (red closed squares) and $R_{g\text{-clay}}$ (blue closed circles) were calculated with eqn (38) and eqn (40), respectively, using the values of parameters obtained in the simulation (Table S14†). Error bars are standard deviations of the two values: one is calculated for the results with the small basins and the other is calculated for the results with the large basins.

constant of I_2 between the surface and the interior of clay samples. This equal destabilization might be the reason that the loss ratios for the latter three clay samples increased with RH between 50% and 80% (Fig. 7 and 11) as discussed below (see eqn (40)).

When uptake of I_2 proceeded at a constant rate at low concentrations of I_2 such as the concentrations in the atmosphere, we calculated the uptake rate k_{g0} of I_2 by fresh clays with eqn (37) (see the ESI†)

$$k_{g0} = \frac{\frac{q_\infty}{B_{pm}}k_{loss\text{-}s}(t)}{\frac{1}{K_{ads}} + \frac{1}{\frac{k_{ma}}{K_{pads}k_{loss\text{-}p}} + \frac{k_{ma}}{k_{2f}}} + \frac{k_{loss\text{-}s}(t)}{k_{ma}}} + \frac{\frac{q_\infty}{B_{pm}}}{\frac{q_\infty}{B_{pm}}\frac{1}{k_{ma}} + \frac{1}{K_{ads}k_f} + \frac{1}{K_{ads}K_{pads}k_{loss\text{-}p}} + \frac{k_{loss\text{-}s}(t)}{k_{ma}k_f}\left(\frac{k_f}{K_{pads}k_{loss\text{-}p}} + 1\right)} \quad (37)$$

Because the term k_{ma}^{-1} on the right side of eqn (37) corresponds to mass transfer in a gas-film layer, the surface resistance above fresh clays, $R_{g\text{-clay-0}}$, is represented by

$$R_{g\text{-clay-0}} = \left(\frac{q_\infty}{B_{pn}}K_{ads}k_{loss\text{-}s}(t) + \frac{\frac{q_\infty}{B_{pn}}}{\frac{1}{K_{ads}k_f} + \frac{1}{K_{ads}K_{pads}k_{loss\text{-}p}}}\right)^{-1} \quad (38)$$

We assumed that $k_{loss\text{-}s}(t) = 0$ for clays in the environment because surface active sites might be consumed by exposure to

naturally-occurring I_2 and other species. For clays with $k_{loss\text{-}s}(t) = 0$, the uptake rate k_g of I_2 by the clays and the surface resistance for I_2 above the clays, $R_{g\text{-clay}}$, are given by eqn (39) and (40), respectively, from eqn (37) and (38).

$$k_g = \frac{\frac{q_\infty}{B_{pn}}}{\frac{q_\infty}{B_{pm}}\frac{1}{k_{ma}} + \frac{1}{K_{ads}k_f} + \frac{1}{K_{ads}K_{pads}k_{loss\text{-}p}}} \quad (39)$$

$$R_{g\text{-clay}} = \frac{B_{pn}}{q_\infty}\frac{1}{K_{ads}k_f} + \frac{B_{pn}}{q_\infty}\frac{1}{K_{ads}K_{pads}k_{loss\text{-}p}} \quad (40)$$

Values of k_{g0}, $R_{g\text{-clay-0}}$, k_g, and $R_{g\text{-clay}}$ were calculated from the values of the parameters obtained in the simulation (Table S14†). The calculated values of $R_{g\text{-clay-0}}$ and $R_{g\text{-clay}}$ are plotted in Fig. 11. The $R_{g\text{-clay-0}}$ values were greater than the $R_{g\text{-a-clay}}$ values for run 1 and the difference was about 100 s m^{-1} for illite and AgroMAT-AG-1 samples. The implication is that the value of $R_{g\text{-cont}}$ in eqn (30) was overestimated. It is possible that the value of

1054 | Environ. Sci.: Atmos., 2022, 2, 1041–1059

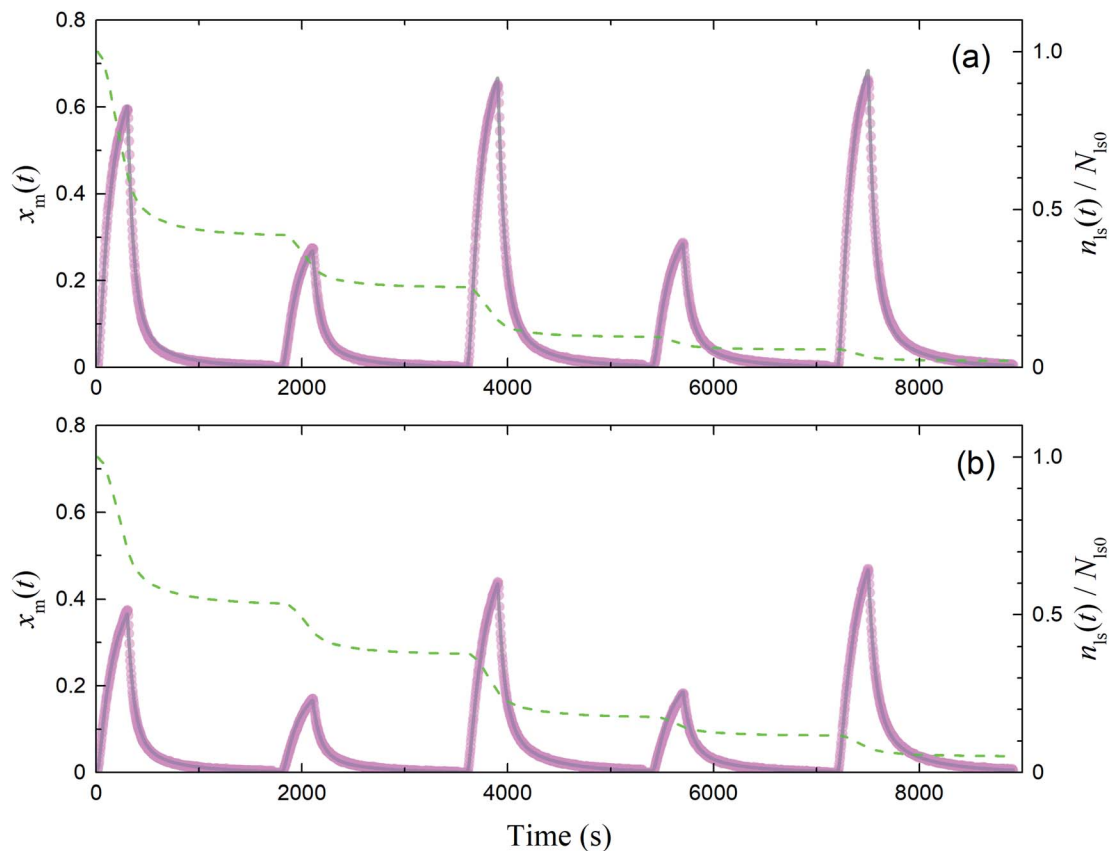© 2022 The Author(s). Published by the Royal Society of Chemistry

Fig. 12 Time series of $x_m(t)$ in I_2–air(s) observed (pink circles) and simulated (grey curves) in runs 1–5 with each montmorillonite sample at 80% RH in (a) small basins (S/S_c, 0.187) and (b) large basins (S/S_c, 0.461). Green dashed curves indicate the time series of residence ratios of active sites for I_2 loss, $n_{ls}(t)/N_{ls0}$. Temporal duration of each run was about 1700 s and there were several minutes between runs; however, each panel shows plots of all data from runs 1–5 in consecutive 1800 s intervals for convenience.
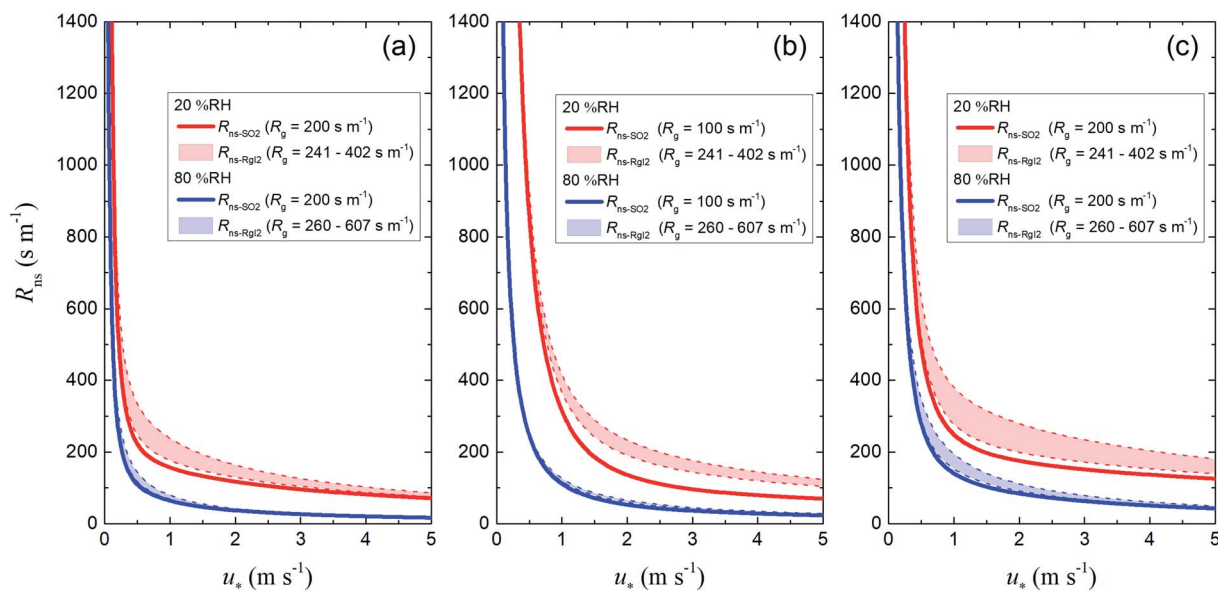

Fig. 13 Plots of non-stomatal surface resistance, R_{ns}, against friction velocity, u_*, at 20% RH (red) and 80% RH (blue) if R_g is the reference value for SO_2 (solid curves, R_{ns-SO2}) or the R_{g-clay} value for I_2 (dashed curves, $R_{ns-RgI2}$) for (a) short grass and forbs, (b) evergreen broadleaf trees, and (c) deciduous broadleaf trees. For the deciduous broadleaf tree LUC, LAI is 0.5, the reference value of LAI in March (see the ESI†).

$R_{g\text{-cont}}$ was smaller than the value of $R_{g\text{-cont-w}}$ because the surface roughness of clay samples decreased resistance to mass transfer in the gas-film layer. For the same reason, the $R_{g\text{-clay}}$ values were greater than the $R_{g\text{-a-clay}}$ values for run 5. This also resulted from the fact that, even at the end of the injection period in run 5, $k_{1\text{-a}}(t)$ did not decrease to a constant value which corresponded to the value expressed using eqn (40).

Fig. S18 and S19† show the plots of $B_{nq}/q_\infty/K_{ads}$, r_1, and r_2 against RH for each clay sample in small basins (Fig. S18†) and large basins (Fig. S19†) where r_1 and r_2 are the first term and the second term, respectively, in the right of eqn (40). Fig. S18 and S19† show that values of $B_{pn}/q_\infty/K_{ads}$ decreased with RH between 50% and 80% for all clay samples. It meant that the adsorption of I_2 on the surfaces of clay samples increased with increasing RH. Hence if k_f, K_{pads}, and $k_{loss\text{-p}}$ were constant,

values of r_1 and r_2 would decrease with increasing RH and the loss ratios would increase for all clay samples. However, r_1 or r_2 or both increased with increasing RH for illite, allophane, and kaolinite samples because K_{pads} decreased with increasing RH. In contrast, values of K_{pads} increased or remained almost constant and the loss ratios increased with increasing RH between 50% and 80% for montmorillonite, halloysite, and AgroMAT AG-1. It suggested that relative humidity might destabilize I_2 in the interior more than on the surface for the former three clay samples and to almost the same extent as on the surface for the latter three clay samples. This difference might come from the difference in pH values of the water film in the interiors and buffering capacity against absorption of CO_2 among the clay samples.
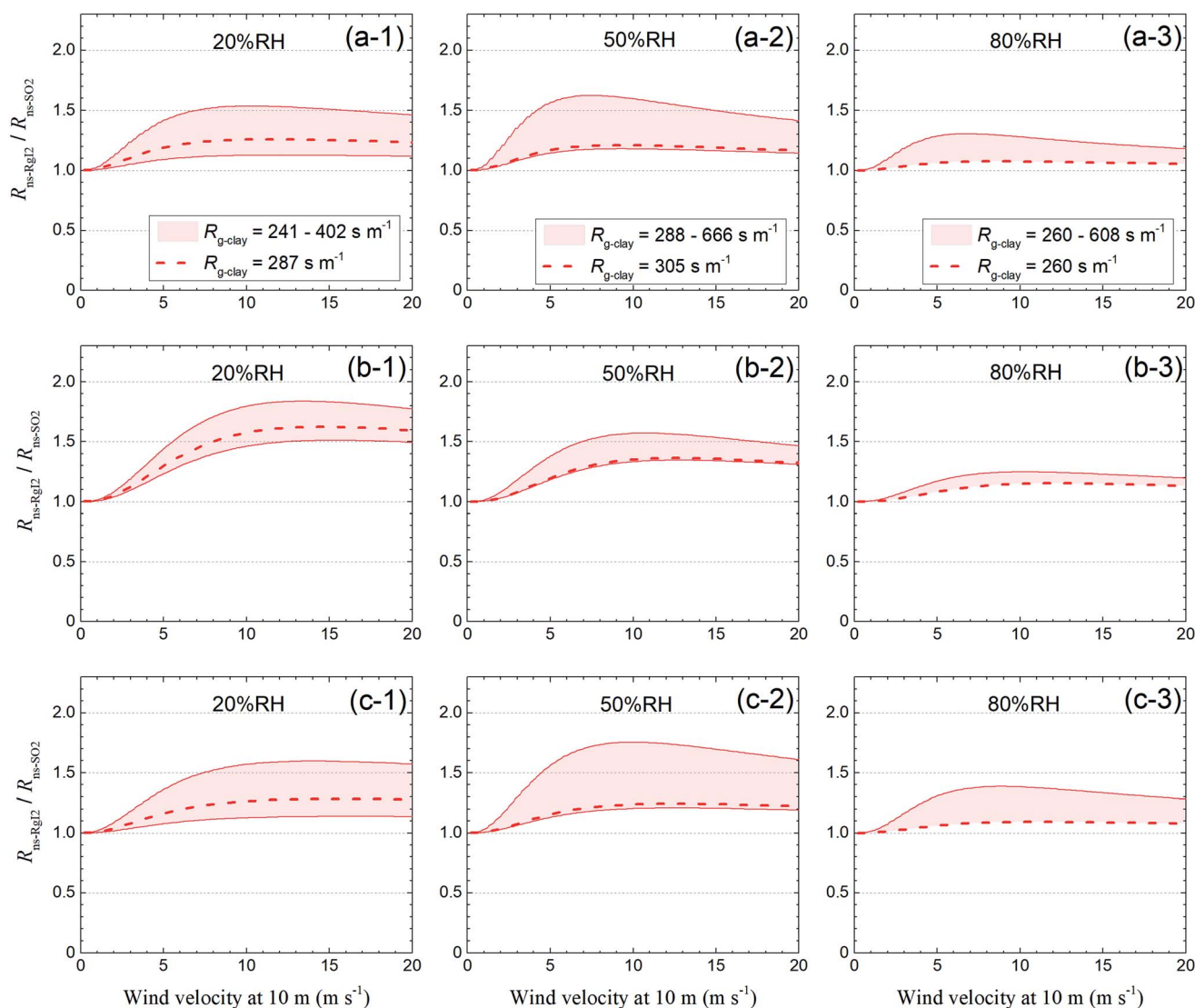

Fig. 14 $R_{ns\text{-RgI2}}/R_{ns\text{-SO2}}$ *versus* wind velocity at 10 m of height at (1) 20% RH, (2) 50% RH, and (3) 80% RH for (a) short grass and forbs, (b) evergreen broadleaf trees, and (c) deciduous broadleaf trees. Red regions indicate values calculated from the range of the $R_{g\text{-clay}}$ values. Dashed curves indicate values calculated from the $R_{g\text{-clay}}$ values above the AgroMAT AG-1 sample. The reference values of R_g for SO_2 are 100 s m^{-1} for evergreen broadleaf tree LUCs and 200 s m^{-1} for the other LUCs. For deciduous broadleaf tree LUCs, roughness length, z_0, is set at 0.4 m and *LAI* is 0.5, the reference value of LAI in March (see the ESI†).

Values of $R_{g\text{-clay}}$ for all samples reached 241–402 s m^{-1} at 20% RH, 288–666 s m^{-1} at 50% RH, and 260–608 s m^{-1} at 80% RH. These values were equal to a value of 330 s m^{-1}, which corresponded to a deposition velocity of 0.3 cm s^{-1} in atmospheric model calculations for I_2^{model}, within a factor of two. However, if the clay content in soils, such as 10–20% in weight,[44,45] was taken into account, the surface resistance for I_2 with respect to uptake by clay minerals further exceeded the values used in the atmospheric models. We used the $R_{g\text{-clay}}$ values calculated from eqn (40) to estimate non-stomatal bulk surface resistance in dry deposition (Section 3.4).

3.4 Influence of I_2 uptake by clay minerals on non-stomatal resistance for I_2 above ground surfaces

We estimated non-stomatal resistance for I_2 above ground surfaces (R_{ns}) with eqn (1) using the R_g values for I_2 above the clay minerals that we examined. The values of R_{ac} and R_{cut} in eqn (1) have been expressed as functions of friction velocity (u_*) and the leaf area index (LAI), both of which have been specified for each land use category (LUC) for dry and wet conditions.[20] Because the RH range in this study (20–80% RH) fell within the range of dry conditions, we calculated R_{ac} and R_{cut} values under dry conditions with eqn (41) and (42), respectively:

$$R_{ac} = \frac{R_{ac0}\text{LAI}^{1/4}}{u_*^2} \tag{41}$$

$$R_{cut} = \frac{R_{cut0}}{e^{0.03\text{RH}}\text{LAI}^{1/4}u_*} \tag{42}$$

where R_{ac0} is the reference value for in-canopy aerodynamic resistance specific to each LUC and R_{cut0} is the reference value for cuticle resistance under dry conditions specific to both depositing species and the LUC. Table S16† lists reference values of R_{ac0}, R_{cut0} for SO_2, R_g for SO_2, and LAI for three LUCs (short grass and forbs, evergreen broadleaf trees, and deciduous broadleaf trees).[20]

For soils in each LUC, we calculated R_{ns} values (1) using the reference value of R_g for SO_2 as the ground surface resistance ($R_{ns\text{-SO2}}$) and (2) using the $R_{g\text{-clay}}$ values for I_2 above the clay samples as ground surface resistance ($R_{ns\text{-RgI2}}$). Fig. 13 shows plots of these resistances against u_* at 20% RH and 80% RH. The $R_{ns\text{-RgI2}}$ values were calculated from the minimum and maximum $R_{g\text{-clay}}$ values for I_2 for all the clay samples. Values of $R_{ns\text{-RgI2}}$ consistently exceeded those of $R_{ns\text{-SO2}}$; the difference between them was smaller at 80% RH than at 20% RH because the R_{cut} values for SO_2 decreased with increasing RH, as seen in eqn (42), and R_{ns} was thereby more strongly controlled by R_{cut} than by R_g (eqn (1)).

Fig. 14 shows the ratio of these two resistances ($R_{ns\text{-RgI2}}/R_{ns\text{-SO2}}$) for each LUC at 20% RH, 50% RH, and 80% RH against wind velocity at a height of 10 m (u_{10}), which was calculated by relating u_{10} to u_* with eqn (S37).† For the short grass and forb LUCs, the $R_{ns\text{-RgI2}}/R_{ns\text{-SO2}}$ ratios at $u_{10} = 5$ m s^{-1} were approximately 1.1–1.4 at 20% RH, 1.1–1.6 at 50% RH, and 1.1–1.3 at 80% RH, whereas the values of $R_{g\text{-clay}}$ were approximately 1.2–3.3 times the reference value of R_g for SO_2 above soils in this LUC (200 s m^{-1}). For the evergreen broadleaf tree LUC, the dependence of the $R_{ns\text{-RgI2}}/R_{ns\text{-SO2}}$ ratios on wind velocity was greater than for the short grass and forb LUCs because the roughness length was longer in the former than in the latter. The $R_{ns\text{-RgI2}}/R_{ns\text{-SO2}}$ ratios at $u_{10} = 10$ m s^{-1} were approximately 1.5–1.8 at 20% RH, 1.3–1.6 at 50% RH, and 1.1–1.2 at 80% RH whereas the values of $R_{g\text{-clay}}$ were approximately 2.4–6.6 times the reference value of R_g for SO_2 above soils in this LUC (100 s m^{-1}). For the deciduous broadleaf tree LUC, the $R_{ns\text{-RgI2}}/R_{ns\text{-SO2}}$ ratios at $u_{10} = 10$ m s^{-1} were approximately 1.1–1.6 at 20% RH, 1.2–1.8 at 50% RH, and 1.1–1.4 at 80% RH. Fig. 14 also shows the $R_{ns\text{-RgI2}}/R_{ns\text{-SO2}}$ ratios calculated from the $R_{g\text{-clay}}$ values above the AgroMAT AG-1 sample (dashed curves). Values of this ratio at 80% RH were as much as 1.2 for all LUCs. Values of this ratio became greater at lower relative humidity and the values at 20% RH were as much as 1.6 for the evergreen broadleaf tree LUC and as much as 1.3 for the other LUCs. The change in R_{ns} by switching the R_g values between I_2 and SO_2 in the scaling method could thus be appreciable at 20% RH.

4.   Conclusion

We used the rectangular pulse method with an IBBCEAS instrument to determine uptake rates of I_2 by aqueous solutions and clay particles in a gas mixture of 400 ppmv CO_2 and humidified air at 283 K. Uptake of I_2 proceeded much more rapidly by aqueous ascorbic acid than by water; the former was limited by mass transfer in the gas-film layer. Reactions of I_2 with ascorbic acid were expected to proceed in the leaf interior. However, this would happen only in the small number of plants that open their stomata at night.

Uptake of I_2 by clay particles was confirmed at 20–80% RH. Uptake rates of I_2 varied among the clay samples, but the variation was small compared to that of the BET surface areas of the samples. Uptake rates of I_2 decreased with successive runs and remained finite through each set of experimental runs. These finite rates decreased with increasing relative humidity from 20% RH to 80% RH for illite, allophane, and kaolinite samples. This dependence on relative humidity was different from that for SO_2, a commonly used proxy for I_2 in scaling methods. Ratios of I_2 loss and adsorption decreased and increased, respectively, with the exposure time of clay samples to I_2 and their changes were largest during the initial periods after exposure to I_2. Confirmation of the uptake of I_2 by clay minerals at 20–80% RH suggested that it contributed to the dry deposition of I_2 on soils as much as other processes such as reactions of I_2 with organic matter. Uptake of I_2 by clay samples probably proceeded through irreversible adsorption of I_2 in micropores of clay minerals, as reported for I_2 uptake by active carbons.[40]

The time-series of I_2 were reproduced in the simulation by assuming a two-stage process. The parameters obtained in the simulation were used to estimate I_2 uptake rates at low concentrations of I_2 that might be found in the atmosphere. For fresh clay samples, the surface resistance for I_2 above them was smaller than that for I_2^{model} above soils applied to atmospheric model calculations, such as 200 s m^{-1}. For clay samples having been exposed to a gas mixture of I_2, the surface resistance,

© 2022 The Author(s). Published by the Royal Society of Chemistry

Environ. Sci.: Atmos., 2022, **2**, 1041–1059 | **1057**

however, exceeded the values used in atmospheric models. Further excess was expected by taking into account the clay content in soils. For vegetated surfaces such as those near the Fukushima Dai-ichi nuclear power plant, the change in R_{ns} by switching the R_g values between I_2 and SO_2 in the scaling method was smaller at 80% RH than at 20% RH, and it could be appreciable at 20% RH. For vegetated surfaces, switching the R_g values between I_2 and SO_2 in the scaling method thus remained useful for estimating the dry deposition velocity of I_2 at 80% RH, but it might result in substantial errors for the surface resistance at 20% RH, unless surface resistance for I_2 above soils is controlled by other processes such as reactions of I_2 with organic matter in soils. This suggested that the dry deposition processes of I_2 or I_2^{model} needed to be estimated separately before and after sunrise when I_2 was released at night.

In the blank experiments (Section 3.1), the loss and adsorption of I_2 on inert surfaces (PTFE wall surfaces) increased with increasing RH. This pattern was similar to the pattern of R_{cut} for SO_2, as expected from eqn (42). As seen in Fig. 13, R_{ns} values above vegetated surfaces at 80% RH were determined mostly by R_{cut} rather than by R_g. The estimate of R_{cut} for I_2 was thus important for evaluating the dry deposition velocity of I_2 at night. A study on R_{cut} was, however, beyond the scope of this work. Although we did not explicitly drive dry deposition velocities in this study, the surface resistance data we obtained can be used in series-resistance models of dry deposition embedded in atmospheric transport and dispersion models to assess the human risk of radioiodine.

Author contributions

The laboratory experiments and simulated calculations were performed by SK. The manuscript was written through the contributions of all authors. All authors have given approval to the final version of the manuscript.

Conflicts of interest

There are no conflicts of interest to declare.

Acknowledgements

References

1 WHO, *Health Effects of the Chernobyl Accident and Special Health Care Programmes*, Geneva, 2006.

2 G. Katata, M. Chino, T. Kobayashi, H. Terada, M. Ota, H. Nagai, M. Kajino, R. Draxler, M. C. Hort, A. Malo, T. Torii and Y. Sanada, Detailed source term estimation of the atmospheric release for the Fukushima Daiichi Nuclear Power Station accident by coupling simulations of an atmospheric dispersion model with an improved deposition scheme and oceanic dispersion model, *Atmos. Chem. Phys.*, 2015, **15**, 1029–1070.

3 Y. Morino, T. Ohara and M. Nishizawa, Atmospheric behavior, deposition, and budget of radioactive materials from the Fukushima Daiichi nuclear power plant in March 2011, *Geophys. Res. Lett.*, 2011, **38**, L00G11.

4 K. Saito, I. Tanihata, M. Fujiwara, T. Saito, S. Shimoura, T. Otsuka, Y. Onda, M. Hoshi, Y. Ikeuchi, F. Takahashi, N. Kinouchi, J. Saegusa, A. Seki, H. Takemiya and T. Shibata, Detailed deposition density maps constructed by large-scale soil sampling for gamma-ray emitting radioactive nuclides from the Fukushima Dai-ichi Nuclear Power Plant accident, *J. Environ. Radioact.*, 2015, **139**, 308–319.

5 H. Tsuruta, Y. Moriguchi and T. Nakajima, Dynamics of atmospheric ^{131}I in radioactive plumes in eastern Japan immediately after the Fukushima accident by analysing published data, *Sci. Rep.*, 2019, **9**, 13240.

6 Y. Muramatsu, H. Matsuzaki, C. Toyama and T. Ohno, Analysis of ^{129}I in the soils of Fukushima Prefecture: preliminary reconstruction of ^{131}I deposition related to the accident at Fukushima Daiichi Nuclear Power Plant (FDNPP), *J. Environ. Radioact.*, 2015, **139**, 344–350.

7 A. C. Chamberlain and R. C. Chadwick, Deposition of airborne radioiodine vapor, *Nucleonics*, 1953, **11**, 22–25.

8 A. C. Chamberlain, A. E. J. Eggleton, W. J. Megaw and J. B. Morris, Behaviour of iodine vapour in air, *Discuss. Faraday Soc.*, 1960, **30**, 162–169.

9 A. C. Chamberlain and R. C. Chadwick, Transport of iodine from atmosphere to ground, *Tellus*, 1966, **18**, 226–237.

10 O. Telly Bah, D. Hebert, O. Connan, L. Solier, P. Laguionie, D. Bourlès and D. Maro, Measurement and modelling of gaseous elemental iodine (I_2) dry deposition velocity on grass in the environment, *J. Environ. Radioact.*, 2020, **219**, 106253.

11 A. C. Chamberlain, CXXI. Experiments on the deposition of iodine 131 vapour onto surfaces from an airstream, *London, Edinburgh Dublin Philos. Mag. J. Sci.*, 1953, **44**, 1145–1153.

12 M. D. Allen and R. D. Neff, Measurements of deposition velocity of gaseous elemental iodine on water, *Health Phys.*, 1975, **28**, 707–715.

13 N. G. Stewart and R. N. Crooks, Long-range travel of the radioactive cloud from the Accident at Windscale, *Nature*, 1958, **182**, 627–628.

14 G. A. Sehmel, Particle and gas dry deposition: A review, *Atmos. Environ.*, 1980, **14**, 983–1011.

15 A. Saiz-Lopez and J. M. C. Plane, Novel iodine chemistry in the marine boundary layer, *Geophys. Res. Lett.*, 2004, **31**, L04112.

16 A. Saiz-Lopez, J. M. C. Plane, A. R. Baker, L. J. Carpenter, R. von Glasow, J. C. Gómez Martín, G. McFiggans and R. W. Saunders, Atmospheric chemistry of iodine, *Chem. Rev.*, 2012, **112**, 1773–1804.

17 G. Katata, M. Ota, H. Terada, M. Chino and H. Nagai, Atmospheric discharge and dispersion of radionuclides during the Fukushima Dai-ichi Nuclear Power Plant accident. Part I: Source term estimation and local-scale

1058 | *Environ. Sci.: Atmos.*, 2022, **2**, 1041–1059

© 2022 The Author(s). Published by the Royal Society of Chemistry

atmospheric dispersion in early phase of the accident, *J. Environ. Radioact.*, 2012, **109**, 103–113.

18 M. L. Wesely and B. B. Hicks, Some factors that affect the deposition rates of sulfur dioxide and similar gases on vegetation, *J. Air Pollut. Control Assoc.*, 1977, **27**, 1110–1116.

19 R. C. Musselman and T. J. Minnick, Nocturnal stomatal conductance and ambient air quality standards for ozone, *Atmos. Environ.*, 2000, **34**, 719–733.

20 L. Zhang, J. R. Brook and R. Vet, A revised parameterization for gaseous dry deposition in air-quality models, *Atmos. Chem. Phys.*, 2003, **3**, 2067–2082.

21 M. L. Wesely, Parameterization of surface resistances to gaseous dry deposition in regional-scale numerical models, *Atmos. Environ.*, 1989, **23**, 1293–1304.

22 S. Kutsuna and N. Kaneyasu, Henry's law constants and hydration equilibrium constants of n-hexanal and their temperature dependence as determined by the rectangular pulse method, *Chem. Eng. Sci.*, 2021, **239**, 116639.

23 S. Kutsuna, K. Takeuchi and T. Ibusuki, Laboratory study on heterogeneous degradation of methyl chloroform (CH_3CCl_3) on aluminosilica clay minerals as its potential tropospheric sink, *J. Geophys. Res.: Atmos.*, 2000, **105**, 6611–6620.

24 S. Kutsuna, L. Chen, K. Nohara, K. Takeuchi and T. Ibusuki, Heterogeneous decomposition of $CHF_2OCH_2CF_3$ and $CHF_2OCH_2C_2F_5$ over various standard aluminosilica clay minerals in air at 313 K, *Environ. Sci. Technol.*, 2002, **36**, 3118–3123.

25 S. Kutsuna, L. Chen, K. Ohno, N. Negishi, K. Takeuchi, T. Ibusuki, K. Tokuhashi and A. Sekiya, Laboratory study on heterogeneous decomposition of methyl chloroform on various standard aluminosilica clay minerals as a potential tropospheric sink, *Atmos. Chem. Phys.*, 2003, **3**, 1063–1082.

26 S. E. Fiedler, A. Hese and A. A. Ruth, Incoherent broad-band cavity-enhanced absorption spectroscopy, *Chem. Phys. Lett.*, 2003, **371**, 284–294.

27 R. A. Washenfelder, A. O. Langford, H. Fuchs and S. S. Brown, Measurement of glyoxal using an incoherent broadband cavity enhanced absorption spectrometer, *Atmos. Chem. Phys.*, 2008, **8**, 7779–7793.

28 C. Bahrini, A.-C. Grégoire, D. Obada, C. Mun and C. Fittschen, Incoherent broad-band cavity enhanced absorption spectroscopy for sensitive and rapid molecular iodine detection in the presence of aerosols and water vapour, *Opt. Laser Technol.*, 2018, **108**, 466–479.

29 *FACT (Free-Access Chemometric Toolbox) under SCILAB*, https://atoms.scilab.org/toolboxes/FACT, accessed April, 2022.

30 *SCILAB*, https://www.scilab.org, accessed April, 2022.

31 P. Spietz, J. Gómez Martín and J. P. Burrows, Effects of column density on I_2 spectroscopy and a determination of I_2 absorption cross section at 500 nm, *Atmos. Chem. Phys.*, 2006, **6**, 2177–2191.

32 H. Keller-Rudek, G. K. Moortgat, R. Sander and R. Sörensen, The MPI-Mainz UV/VIS Spectral Atlas of Gaseous Molecules of Atmospheric Interest, *Earth Syst. Sci. Data*, 2013, **5**, 365–373.

33 F. A. Morrissey and M. E. Grismer, Kinetics of volatile organic compound sorption/desorption on clay minerals, *J. Contam. Hydrol.*, 1999, **36**, 291–312.

34 A. E. Burgess and J. C. Davidson, Kinetics of the Rapid Reaction between Iodine and Ascorbic Acid in Aqueous Solution Using UV-Visible Absorbance and Titration by an Iodine Clock, *J. Chem. Educ.*, 2014, **91**, 300–304.

35 M. Eigen and K. Kustin, The Kinetics of Halogen Hydrolysis, *J. Am. Chem. Soc.*, 1962, **84**, 1355–1361.

36 A. Takami, T. Kondo, A. Kado and S. Koda, The uptake coefficient of I_2 on various aqueous surfaces, *J. Atmos. Chem.*, 2001, **39**, 139–153.

37 W. Eguchi, M. Adachi and M. Yoneda, Dependency of partition equilibrium of iodine between air and aqueous solution containing sodium hydroxide upon temperature and concentration, *J. Chem. Eng. Jpn.*, 1974, **6**, 389–396.

38 C. R. Reid, J. M. Prausnitz and B. E. Poling, *The Properties of Gases Ana Liquids*, 5th edn, McGraw-Hill, New York, 1987.

39 U. Pöschl and M. Shiraiwa, Multiphase chemistry at the atmosphere–biosphere interface influencing climate and public health in the Anthropocene, *Chem. Rev.*, 2015, **115**, 4440–4475.

40 S. K. Bhatia, F. Liu and G. Arvind, Effect of pore blockage on adsorption isotherms and dynamics: Anomalous adsorption of iodine on activated carbon, *Langmuir*, 2000, **16**, 4001–4008.

41 W. Rudzinski and W. Plazinski, Studies of the kinetics of solute adsorption at solid/solution interfaces: On the possibility of distinguishing between the diffusional and the surface reaction kinetic models by studying the pseudo-first-order kinetics, *J. Phys. Chem. C*, 2007, **111**, 15100–15110.

42 L. Largitte and R. Pasquier, A review of the kinetics adsorption models and their application to the adsorption of lead by an activated carbon, *Chem. Eng. Res. Des.*, 2016, **109**, 495–504.

43 D. Feng, X. Li, X. Wang, J. Li, F. Sun, Z. Sun, T. Zhang, P. Li, Y. Chen and X. Zhang, Water adsorption and its impact on the pore structure characteristics of shale clay, *Appl. Clay Sci.*, 2018, **155**, 126–138.

44 J. Koarashi, M. Atarashi-Andoh, T. Matsunaga, T. Sato, S. Nagao and H. Nagai, Factors affecting vertical distribution of Fukushima accident-derived radiocesium in soil under different land-use conditions, *Sci. Total Environ.*, 2012, **431**, 392–401.

45 K. Fujii, N. Yamaguchi, N. Imamura, M. Kobayashi, S. Kaneko and M. Takahashi, Effects of radiocesium fixation potentials on ^{137}Cs retention in volcanic soil profiles of Fukushima forests, *J. Environ. Radioact.*, 2019, **198**, 126–134.

© 2022 The Author(s). Published by the Royal Society of Chemistry

Environ. Sci.: Atmos., 2022, **2**, 1041–1059 | **1059**